water

MDPI

Article

Dynamics and Drivers of Water Clarity Derived from Landsat and In-Situ Measurement Data in Hulun Lake from 2010 to 2020

Chuanwu Zhao [1,2], Yuhuan Zhang [3,*], Wei Guo [4] and Muhammad Fahad Baqa [5]

[1] State Key Laboratory of Remote Sensing Science, Jointly Sponsored by Beijing Normal University and Institute of Remote Sensing and Digital Earth of Chinese Academy of Sciences, Beijing 100875, China; 202131051034@mail.bnu.edu.cn
[2] Institute of Remote Sensing Science and Engineering, Faculty of Geographical Sciences, Beijing Normal University, Beijing 100875, China
[3] Ministry of Ecology and Environment Center for Satellite Application on Ecology and Environment, Beijing 100094, China
[4] College of Geoscience and Surveying Engineering, China University of Mining and Technology, Beijing 100083, China; weiguo@cumtb.edu.cn
[5] Key Laboratory of Digital Earth Science, Aerospace Information Research Institute, Chinese Academy of Sciences, Beijing 100094, China; 2252293808@mails.ucas.edu.cn
* Correspondence: zhangyh01@radi.ac.cn

Abstract: Water clarity (Secchi disk depth, SDD), as a proxy of water transparency, provides important information on the light availability to the lake ecosystem, making it one of the key indicators for evaluating the water ecological environment, particularly in nutrient-rich inland lakes. Hulun Lake, the fifth largest lake in China, has faced severe water quality challenges in the past few decades, e.g., high levels of phosphorus and nitrogen, leading to lake eutrophication. However, under such a serious context, the temporal and spatial dynamics of SDD in Hulun Lake are still unclear. In this paper, we obtained the best model input parameters by using stepwise linear regression models to test field measurements against remote sensing band information, and then developed the SDD satellite algorithm suitable for Hulun Lake by comparing six models (i.e., linear, quadratic, cubic, exponential, power, and logarithmic). The results showed that (1) B3/(B1 + B4) [red/(blue-near-infrared)] was the most sensitive parameter for transparency (R = 0.84) and the exponential model was the most suitable transparency inversion model for Hulun Lake (RMSE = 0.055 m, MAE = 0.003 m), (2) The annual mean SDD of Hulun Lake was higher in summer than in autumn, the summer SDD decreased from 2010 (0.23 m) to 2020 (0.17 m), and the autumn SDD increased from 2010 (0.06 m) to 2020 (0.16 m). The SDD in the littoral zones of Hulun Lake was less than that in the central part; (3) meteorological conditions (i.e., precipitation and wind speed) were highly correlated with the variation of SDD. Cropland expansion was the possible reason for the low SDD at the entrance of Hulun Lake flow. The findings of this study have important implications for the development and implementation of ecological protection and restoration strategies in the Hulun Lake basin.

Keywords: SDD; landsat; spatio-temporal dynamics; Driving force; Hulun Lake

Citation: Zhao, C.; Zhang, Y.; Guo, W.; Baqa, M.F. Dynamics and Drivers of Water Clarity Derived from Landsat and In-Situ Measurement Data in Hulun Lake from 2010 to 2020. *Water* **2022**, *14*, 1189. https://doi.org/10.3390/w14081189

Academic Editors: Sampsa Koponen and Saku Anttila

Received: 2 March 2022
Accepted: 6 April 2022
Published: 7 April 2022

1. Introduction

Global freshwater resources account for only three percent of the total water resources. China with 18.5% of the world's population, has only 7.7% of freshwater resources [1]. Lakes provide critical ecological and social services to humans and other organisms. Over the past several decades, China's rapid economic development has taken place at the expense of the environment [2,3]. The widespread deterioration of surface

water quality in inland water bodies represents one of the most serious environmental threats to human health and ecosystem services [3,4]. Water clarity (Secchi disk depth, SDD), as a proxy of water transparency, provides important information on the light availability to the lake ecosystem [5,6], making it one of the key indicators for evaluating lake trophic state, particularly in nutrient-rich inland lakes.

SDD is a combined measurement of the scattering and absorption of light in a body of water using a Secchi disk (SD). The SD is weighted and divided into alternating quadrants of black and white [6]. The SD is placed in the lake until the depth at which the tester can no longer see, called the SDD, which is a scientific estimate of water clarity [5,7]. SDD in-situ measurements are easy to implement and therefore attractive in citizen science monitoring programs. However, it is typically costly and time-consuming, limiting its application in remote and treacherous areas [8,9]. In addition, the SDD of inland waters is often inhomogeneous at both space and time scales, which makes it extremely difficult for traditional field sampling methods to fully capture their changing characteristics [10]. Remote sensing, which has the advantages of rapid, spatially continuous, and repeatable observations, has become an important technology for SDD monitoring and assessments and is widely used worldwide [11–14]. Remote sensing algorithms for SDD can be generally classified into the following three categories: empirical, analytical, and semi-analytical algorithms. The first category consists of empirical algorithms established based on the relationship between single or combined bands and SDD [10,15–17]. The second and third types are based on the radiative transfer equation theory [18–20]. According to reports, the optical properties of inland waters are often complex, making it challenging for analytical and semi-analytical algorithms to derive SDD directly from the remote sensing reflectance [10,21].

Remote sensing investigations of major lakes such as Taihu Lake [5,6], Qiandao Lake [8], Hongze Lake [10], Poyang Lake [13], Dianchi Lake, and Chao Hu Lake have also been conducted in China [1,3]. It can be seen that, so far, remote sensing technology has been mainly used to measure water quality in the large lakes of east-central China. Hulun Lake is known as the "kidney of grassland" in Hulunbuir city, the fifth largest lake in China and the largest freshwater lake in the arid region of central Asia [22,23]. Hulun Lake is rich in flora and fauna, abounds in more than 30 species of fish, and is a large fishing ground in Inner Mongolia, China. In addition, Hulun Lake is an important habitat for birds and is an important migration route for birds in northern China. Hulun Lake is extremely important to the ecological protection and soil conservation of the surrounding areas [23,24]. A number of recent studies demonstrate that lakes all over the world have experienced dramatic environmental and climatic changes [5,25–27]. Over the past decades, Hulun Lake has also faced severe water quality challenges, e.g., high levels of phosphorus and nitrogen, leading to lake eutrophication. To develop and implement ecological conservation and restoration strategies, accurately estimating water quality and exploring the drivers of water quality change is critical. The current research on Hulun Lake mainly focuses on total phosphorus (TP) [22], water volume [23], water heat flux [24], aquatic vegetation, etc. Water transparency provides important information on the light availability to the lake ecosystem, making it one of the key indicators for evaluating the water ecological environment, particularly in nutrient-rich inland lakes. However, the temporal and spatial dynamics of SDD in Hulun Lake is still unclear. Moreover, there is a lack of quantitative analysis on the driving factors of SDD changes in Hulun Lake. This does not match the current development concept of "lucid waters and lush mountains are invaluable assets" proposed by the Chinese government and the comprehensive management plan of the water ecology in Hulun Lake. To address this need, we used Landsat data from 2010 to 2020 to study the spatio-temporal distribution of SDD in Hulun Lake to determine the effects of climate change and human activities (see Figure 1).

The main research components were as follows: (1) to develop a practical algorithm to estimate SDD using satellite data suitable for Hulun Lake; (2) to retrieve the spatial and temporal patterns of SDD in Hulun Lake; (3) to analyze the effects of climatic factors

(temperature, precipitation, and wind speed) on the formation and transformation of SDD spatial patterns in Hulun Lake; (4) to explore the influence of human activities on inter-annual changes in SDD in Hulun Lake. The long-term remote sensing inversion of SDD in Hulun Lake is expected to provide a certain theoretical basis and technical reference for its ecological management and sustainable development and lay a solid foundation for the long-term continuous and dynamic monitoring of water quality.

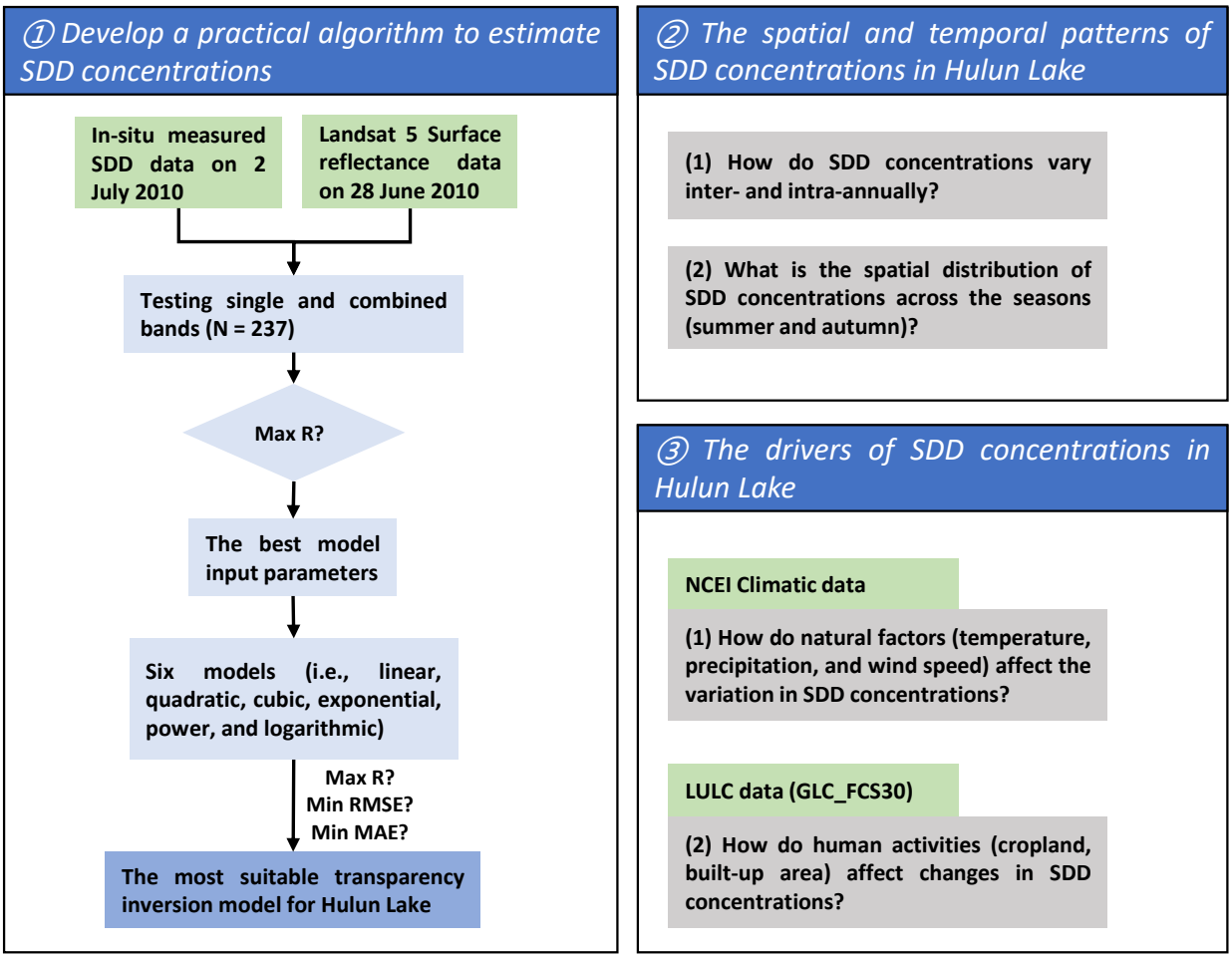

Figure 1. Flowchart diagram of methodology. Note, R represents the Pearson correlation coefficient, RMSE represent the root mean square error, and MAE represents the mean absolute error.

2. Materials and Methods

2.1. Study Area

Hulun Lake is a shallow lake located in the northern part of Inner Mongolia, China (Figure 2a). The elevation of the lake is about 545 m above sea level. The length and width of the lake are 93 km and 32 km, respectively. The lake's depth is about 5–8 m, and the water storage capacity is 14 billion m^3. Hulun Lake is located in the middle temperate zone and belongs to the continental steppe climate zone [23,27]. The region is dry and windy in spring and winter, with low temperatures. In the summer, it is warm with frequent rainfall. In autumn, it cools quickly and has early frosts. In addition, Hulun Lake is one of the lakes with the longest freezing periods in China, with its ice layer more than 1 m thick. Hulun Lake starts to freeze in early November and thaws in early May of the following year. The freezing period is about 180 days. In this paper, we selected the Hulun Lake basin to explore the driving factors (Figure 2b). The Hulun Lake basin is approximately 50 km buffer around Hulun Lake, covering an area of 2,042,283 square kilometers. The Klulun and Urxun rivers supply water to recharge Hulun Lake, which then flows

through the northeastern part of Hulun Lake to the Hulunbuir Steppe downstream. In the past decades, the poor water quality of Hulun Lake's has exacerbated the environmental risks in the basin and posed a severe threat to the sustainable development of the region [23,27]. According to the report of the Ministry of Ecology and Environment, compared with 2015, although the total nitrogen and permanganate indexes of Hulun Lake water quality decreased from 2016 to 2020, the indexes of COD, TP, and fluoride increased, posing a threat to the safety of water sources and soil in downstream crop growing areas. The Chinese government approved the "Implementation Plan for Phase I of the Hulun Lake Basin Ecological and Environmental Comprehensive Management Project (2016–2017)" to implement projects for grassland ecological protection, wetland ecosystem restoration, water conservancy construction, environmental remediation, and management capacity [23,28]. In general, the water history (specifically, long-term exposure to ecological degradation of the lake due to salinization and alkalinization) and the current status of Hulun Lake provide an excellent opportunity for researchers to study water quality issues in the region.

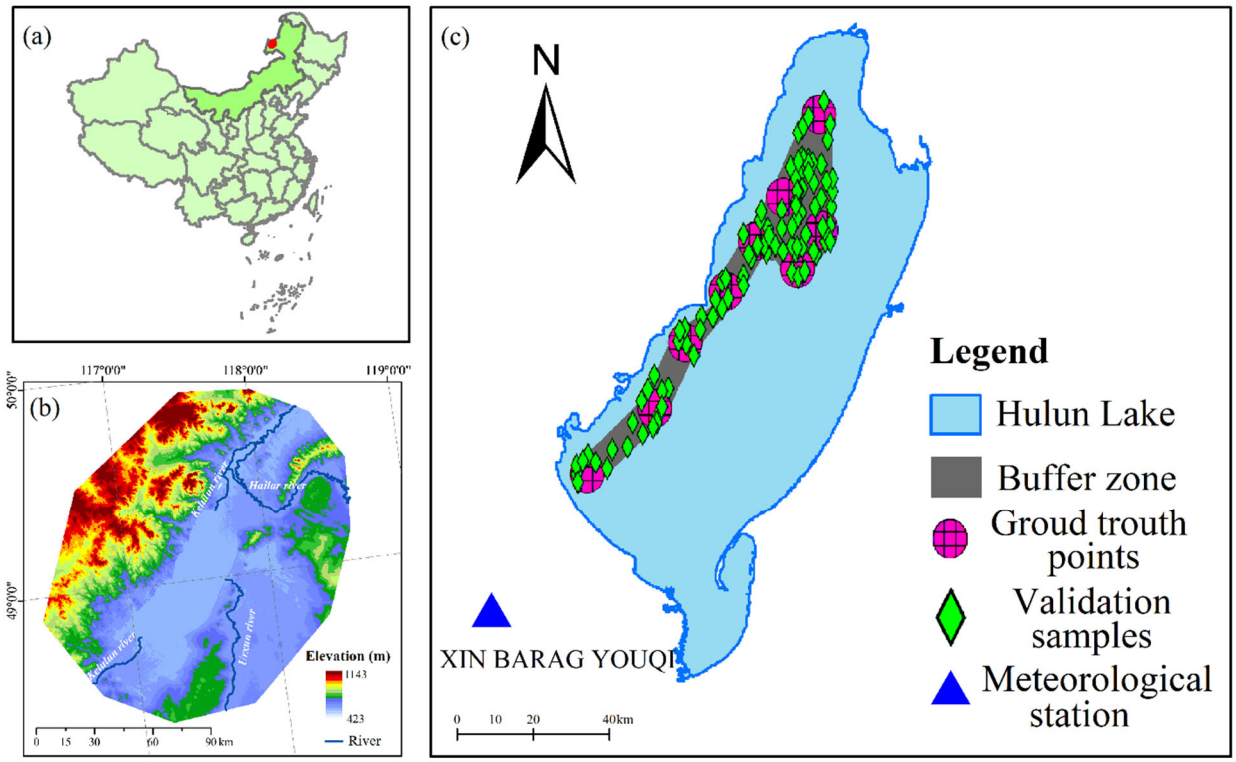

Figure 2. The location of the study area. (**a**) the geographical location of the study area; (**b**) the elevation of the study area; (**c**) the distribution of meteorological stations and field points.

2.2. Data

According to the report, pH, transparency, and dissolved oxygen (DO) are the most important indicators of eutrophication affecting water quality in Hulun Lake [29]. Of these, SDD indicators can be easily measured in the field and can vary more significantly in the remote sensing spectrum. In this study, the in-situ measured SDD data on 2 July 2010, was obtained from the Lake-Watershed Science Sub center, National Earth System Science Data Center, National Science & Technology Infrastructure of China (http://lake.geodata.cn, accessed on 7 May 2021). The measurement manual shows that (1) the weather on the day of the field measurements was clear and the measurements were taken in sunshine, (2) the measurements were taken between 9 a.m. and 12 a.m. (BST), and (3) each measurement point was repeated three times and the average value was selected as the final recorded value. The in-situ measured SDD data were used to develop

and validate the remote sensing inversion model. Landsat data (including TM, ETM+, and OLI images) with a spatial resolution of 30 m were obtained from the United States Geological Survey (https://earthexplorer.usgs.gov/, accessed on 17 October 2021). We downloaded ice-free period images (i.e., summer and fall) from 2010 to 2020. All images were processed to L2T-level (e.g., passed the corrections for topography and radiation) and geometrically registered with less than one-pixel errors. The nearest neighbor resampling technique was used to resample the Landsat images into a pixel size of 30 m during image-to-image registration. Because of the radiometric differences between the Landsat 8 OLI detector and the previous Landsat detectors, we performed a bias correction on Landsat 8 imagery using a linear regression between the reflectance values of each band between Landsat 7 and Landsat 8 [30,31]. This step reduced the difference between Landsat 7 and Landsat 8, resulting in limited differences between the different sensors throughout the time period. We did not correct potential biases between Landsat 5 and 7 as radiometric differences between these sensors are relatively small [31,32].

To explore the effects of climatic factors and human activities on transparency, climatic data and land use/land cover data were obtained. Climatic data, including daily average temperature (TEMP), daily accumulated precipitation (PRCP), and daily average wind speed (WDSP), were obtained from NOAA's National Centers for Environmental Information (NCEI) (https://www.ncei.noaa.gov/, accessed on 21 December 2021). In this paper, we used the observations of the XIN BARAG YOUQI meteorological station (about 20 km from Hulun Lake, see Figure 2c) as the climate data for the whole study area. Land use and land cover (LULC) data with a spatial resolution of 30 m were developed by Zhang et al. [33]. We downloaded the LULC data (i.e., GLC_FCS30) from 2010 to 2020 from the Data Sharing and Service Portal of the Chinese Academy of Sciences (CAS) (http://data.casearth.cn/en/, accessed on 15 December 2021). Land use was divided into the following seven types: cropland, grassland, wetland, impervious surfaces, bare areas, sparse vegetation, and water bodies. In addition, the DEM from the Shuttle Radar Topography Mission (DEM/SRTM) with a spatial resolution of 30 m was sourced from NASA (https://earthdata.nasa.gov/, accessed on 20 June 2021). All remote sensing data were converted into a uniform projection coordinate system (Albers Conic Equal Area).

2.3. Methods

2.3.1. Water Extraction Methods

Monitoring water bodies accurately is important for subsequent water quality assessment. Various water body mapping approaches have been developed to extract water bodies from multispectral images [34,35]. The method based on the spectral water index, especially the modified normalized difference water index (MDNWI) calculated from the green and shortwave-infrared (SWIR) bands, is one of the most popular methods [36,37]. The index is calculated as follows:

$$\mathrm{MNDWI} = \frac{\rho_{Green} - \rho_{Swir}}{\rho_{Green} + \rho_{Swir}} \quad (1)$$

where ρ_{Green} is the TOA reflectance value of the green band and ρ_{Swir} is the TOA reflectance of the SWIR band. In general, MNDWI is more sensitive to water bodies, which usually absorb more SWIR light; the noise generated by soil, vegetation, and impervious surface areas is inhibited because they reflect more SWIR light [38]. Xu pointed out that an appropriate increase of the MNDWI threshold (>0) can effectively reduce the influence of buildings and shadows and achieve a better extraction effect of the water body range [37,39]. It was confirmed by experimental cases in Lakes Dire and Legedadi in Ethiopia that the accuracy is higher for thresholds greater than 0 (approximately 0.1) when using MNDWI for water extraction in turbid lakes [40]. In this study, a threshold value of 0.1 is used on MNDWI to separate the water information (i.e., the pixel was considered as water when its MNDWI value is greater than 0.1).

2.3.2. Inversion Model Development Methods

The correlation analysis method is used to understand the nature of relationships between two individual variables. Pearson correlation analysis is the most widely used correlation statistic method to measure the degree of the relationship between linearly related variables [41]. The value range of the Pearson correlation coefficient (R) is (0, 1). If the absolute value of R tends to 1, there is a significant correlation between the two variables. If the absolute value of R tends to 0, there is no correlation between the two variables. In addition, we used the coefficient of determination (R^2), root mean square error (RMSE) and mean absolute error (MAE) to evaluate the inversion models' performance. The value of R^2 ranges from 0 to 1. An R^2 score of 1 indicates perfect precision, while a score of 0 indicates that the model has the worst prediction performance. The RMSE and MAE are the statistical values of the error between the predicted value and the observed value [42]. The value range of RMSE is (0, +∞). The value range of MAE is (0, +∞). If the dispersion of the inverse model is high, the values of RMSE and MAE will be enlarged. A model with high R^2, low RMSE, and low MAE is deemed as a suitable model for quantitative inversion [42].

2.3.3. Spatial Trend Analysis Methods

We used the standard deviation ellipse (SDE) model and the mean center (MCen) model to analyze the spatial pattern of SDD. Specifically, it is to explore the directional characteristics of the spatial distribution of transparency, and to analyze the seasonal and inter-annual spatial distribution differences of transparency. The SDE model and MCen model are expressed as [43,44]. The SDE requires the calculation of the MCen of a distribution of points, the angle of rotation of the ellipse, and the SDE along with the x and y coordinates. The SDE is centered on the MCen $(\overline{x}, \overline{y})$, which is given by the following:

$$\overline{x} = \frac{\sum x}{p}, \overline{y} = \frac{\sum y}{p} \tag{2}$$

where x and y are the start longitude and latitude of the SDD, respectively.

The angle of rotation (θ) of the ellipse is given by the following:

$$tan\theta = \frac{(\sum \tilde{x}^2 - \sum \tilde{y}^2) + \sqrt{(\sum \tilde{x}^2 - \sum \tilde{y}^2)^2 + 4(\sum \tilde{x}\tilde{y})^2}}{2\sum \tilde{x}\tilde{y}} \tag{3}$$

where $\tilde{x}$ and $\tilde{y}$ are the deviations of the x and y coordinates from $\overline{x}$ and $\overline{y}$.

The SDE along the $x(\sigma_x)$ and $y(\sigma_y)$ coordinates of the ellipse are given by the following:

$$\sigma_x = \sqrt{\frac{2\sum(\tilde{x}cos\theta - \tilde{y}sin\theta)^2}{p}}, \sigma_y = \sqrt{\frac{2\sum(\tilde{x}sin\theta - \tilde{y}cos\theta)^2}{p}} \tag{4}$$

The equation of the ellipse is given by the following:

$$\left(\frac{x}{\sigma_x}\right)^2 + \left(\frac{y}{\sigma_y}\right)^2 = S \tag{5}$$

where S is the confidence level.

The short axis (Sa), long axis (La), and the ratio of long axis to the short axis (rLSa) of the SDE represent the distribution, range, and spatial trend of SDD, respectively. The rLSa tends to 1, indicating that there is no significant spatial variation in the direction of SDD.

2.3.4. Transparency Estimation Model

Selection of Landsat Spectral Bands

We used Pearson correlation analyze to analysis the correlation between single bands, band combinations, and the in-situ measured SDD data. In total, we tested 12

single bands, 60 sets of two-band combinations, and 165 sets of three-band combinations (see Table A1), and some of the test results are shown in Table 1. The results of the analysis showed that there was a significant correlation between the green and near-infrared reflectance values and the measured SDD values, reaching above −0.7. The correlation between the measured SDD values and the band combinations was significantly improved. Band combinations are more sensitive to the measured SDD values compared to single bands, which is consistent with previous studies [45]. At the significance level of $p < 0.01$, B3/(B1+B4) [red/(blue-near-infrared)] had the highest correlation coefficient (0.841) with the measured SDD values.

Table 1. Correlation coefficient of Landsat-5 TM band combinations with measured SDD.

Band	R	Band	R	Band	R
B1	−0.526	**Ln(B1/B3)**	−0.636	**B1/(B1 + B3)**	−0.634
B2	−0.717 *	**Ln(B2/B3)**	−0.651	**B2/(B2 + B3)**	−0.657
B4	−0.675 *	**Ln(B3/B4)**	0.605	**B4/(B3 + B7)**	−0.654
Ln(B2)	−0.714 *	**B2/(B3 + B7)**	−0.667 *	**B1 * (B2 − B3)/(B2 * B3)**	−0.710 *
Ln(B4)	−0.664	**B3/(B1 + B2)**	0.728 *	**B4 * (B2 − B3)/(B2 * B3)**	−0.710 *
B2/B3	0.667 *	**B3/(B1 + B4)**	0.841 **	**B5*(B2 − B3)/(B2*B3)**	−0.638
B2 − B3	−0.728 *	**B3/(B1 + B7)**	0.692 *	**B7*(B3 − B4)/(B3*B4)**	0.621
B2 − B7	−0.694 *	**B3/(B2 + B4)**	0.672 *	**(B1 − B3)/(B1 + B3)**	−0.634
B4 − B7	−0.698 *	**B3/(B2 + B5)**	0.745 *	**(B2 − B3)/(B2 + B3)**	−0.654
B1 − B3	−0.606	**B3/(B4 + B5)**	0.769 *	**(B3 − B4)/(B3 + B4)**	0.612

−0.75 −0.7 −0.65 −0.6 −0.5 0.6 0.65 0.70 0.75 0.8 0.85

(*): significant correlation for $p < 0.05$. (**): significant correlation for $p < 0.01$.

Development and Validation of Transparency Estimation Algorithms

The data of nine sampling points collected in June 2010 were selected to establish the model (see Figure 2c). In Origin software (OriginLab Corporation, v.2020, Northampton, MA, USA), band combinations (i.e., red/(blue-near-infrared)) and the measured SDD value were set as the independent variable and the dependent variable, respectively. The linear regression model is applicable when (1) there is a linear relationship between the independent variable and the dependent variable, (2) the observations are independent of each other, (3) the residuals follow a normal distribution, and (4) the observations have an equal variance of residuals. The non-linear regression model (e.g., quadratic, cubic) is an extension of the linear regression model, which requires that at least one variable not have an exponent of 1. In practical problems, the regression function is often a non-linear function [46,47]. Six of the models (i.e., linear, quadratic, cubic, exponential, power, and logarithmic models) were chosen for the development of the SDD inversion algorithms. The results showed that the R^2 of all six regression models was greater than 0.6, and the R^2 of the quadratic, cubic, and exponential models was greater than 0.75 (Figure 3). The cubic model was the best fit with an R^2 of 0.839. Also, the results showed that the RMSE of the quadratic, exponential, and cubic models was 0.0317 m, 0.0345 m, and 0.0280 m, respectively. It can be seen that the exponential and cubic model had the smallest MAE values of 0.0267 m and 0.045 m. Thus, it can be seen that the precision of the models developed by choosing (B3)/(B1 + B4) as the band combinations for retrieving SDD values can meet the requirements of remote sensing inversion. Due to the limitation of sample points, the best inversion model was not immediately decided. Also, considering the stability of the inversion models, we validated six models individually.

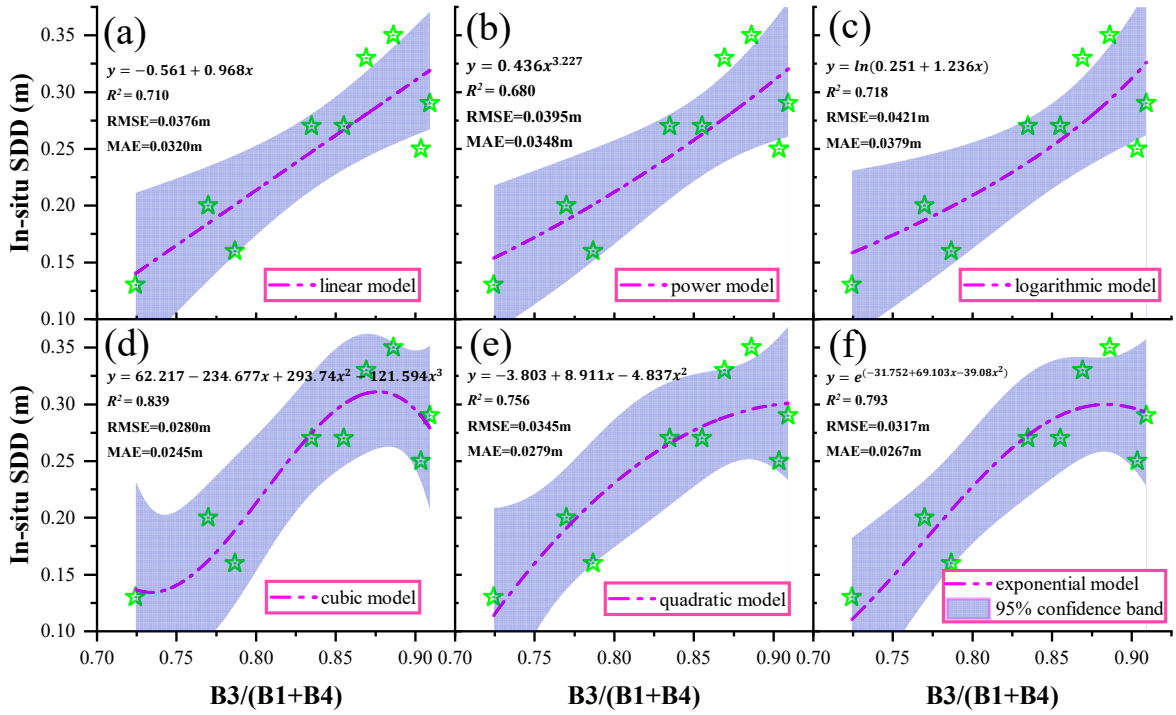

Figure 3. Six regression models were developed between in-situ SDD and B3/(B1+B4), including (**a**) linear; (**b**) power; (**c**) logarithmic; (**d**) cubic; (**e**) quadratic; (**f**) exponential.

The universal kriging interpolation algorithm (Gaussian function as the variogram model) was used to spatially interpolate the in-situ sample points, which is a common method for overcoming the disadvantages of small samples [48,49]. A 100-m buffer zone was created on either side of the in-situ sample points in order to increase the confidence of the samples, and 100 sample points were randomly selected within the buffer zone (see Figure 2c). We set the interpolated values of the kriging algorithm as the true values (i.e., measured SDD) and the calculated values of the six models as the predicted values (i.e., predicted SDD) (Figure 4). The results showed that the cubic model had the smallest R-value and the largest RMSE and MAE values, indicating the high sensitivity and poor stability of the cubic model. The results of the validation of the quadratic and logarithmic models were similar, with R values of 0.5499 and 0.5550, RMSE values of 0.0848 m and 0.1524 m, and MAE values of 0.0072 m and 0.0232 m, respectively. The R values of the linear, power, and exponential models were greater than 0.65. The exponential model had the smallest RMSE and MAE values of 0.0556 m and 0.0030 m. Thus, we used the exponential model (i.e., $y = e^{(-31.752+69.103x-39.08x^2)}$), x denotes the value of red/(blue-near-infrared)) to inverse the values of SDD in the study area.

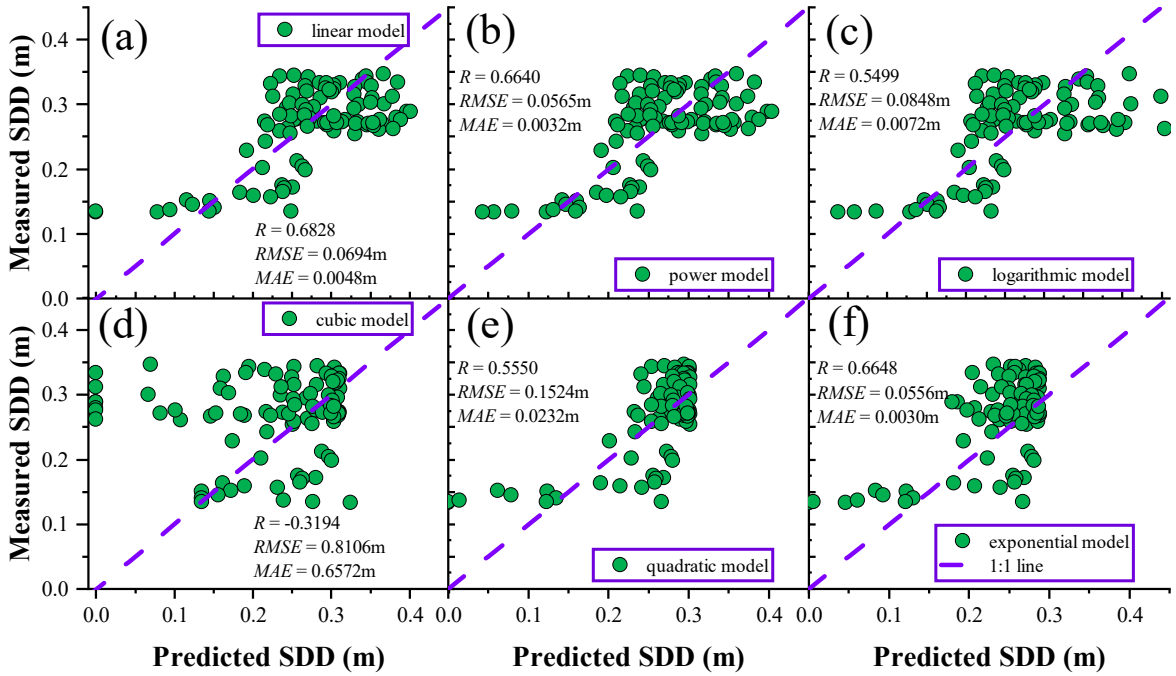

Figure 4. Validation of the accuracy of the inversion models, including (**a**) linear; (**b**) power; (**c**) logarithmic; (**d**) cubic; (**e**) quadratic and (**f**) exponential.

3. Results

3.1. Transparency Mapping and Statistics

Based on the developed exponential SDD inversion model (Exp3P2), water transparency mapping was carried out for the ice-free period (i.e., the summer (June–August) and autumn (September–November) of each year) from 2010 to 2020.

3.1.1. Temporal Characteristics of Transparency

As shown in Figure 5, an overall trend in SDD can be observed in the summer and autumn, despite some fluctuations in certain years. The SDD in the summer had a slow downward trend in Hulun Lake. The SDDs decreased from 0.23 m in 2010 to 0.17 m in 2020, with a decreasing trend of approximately 0.035 m/decade. The minimum value of SDD was 0.09 m, which occurred in 2014. Similarly, there was a fluctuating upward trend in SDD during the autumn, about 0.052 m/decade. The largest value of SDD was recorded in 2015 (0.26 m), with the sudden decrease in SDD occurring in 2016 (0.08 m) and the smallest SDD value in 2017 (0.06). In addition, we found a significant seasonal variation in SDD. Apart from some fluctuations in certain years, the value of SDD was generally greater in summer than in autumn. The reasons for the fluctuations in SDD are described in Section 3.2.

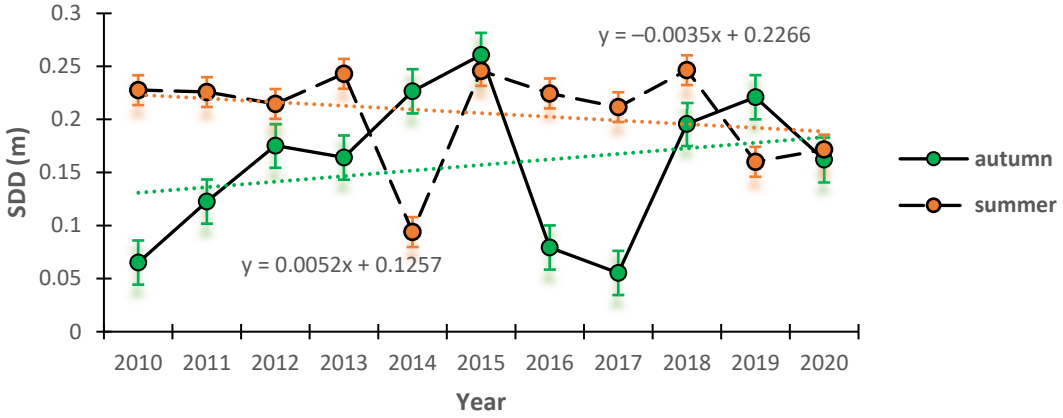

Figure 5. Temporal characteristics of transparency in Hulun Lake from 2010 to 2020.

As shown in Figure 6, the water area of Hulun Lake was approximately 1750 km² between 2010 and 2012. After 2013, the water body began to expand, exceeding 2000 km² from 2014 to 2020. Seasonally, there was no significant difference in the water area between summer and autumn, and the water area in summer was slightly larger than that in autumn. The restoration of the water storage capacity of Hulun Lake was related to the "diversion from river to lake" project and the "river-lake connection" project promoted by the local government. There were significant differences in the proportion of water clarity gradations. Overall, the value of SDD in summer was greater than that in autumn (Figure 6b). In summer, the SDD value of Hulun Lake each year was mainly in the range of > 0.1 m. In 2014, 2019, and 2020, the SDD value was relatively low, mainly between 0.05 m and 0.2 m, with approximately half of the water area in 2014 between 0 and 0.1 m. Except for 2014, 2019, and 2020, more than half of the water area in the remaining years has an SDD greater than 0.2 m. In the years of 2010, 2013, 2015, and 2018, more than half of the water area had an SDD greater than 0.25 m. In autumn, more than half of the area of water had an SDD value greater than 0.2 m in 2012, 2014, 2015, 2018, and 2019, with more than half of the area of water having an SDD value greater than 0.25 m in 2014, 2015, and 2019. In the years 2010, 2016, and 2017, more than half of the water bodies had an SDD value in the range of 0—0.1 m.

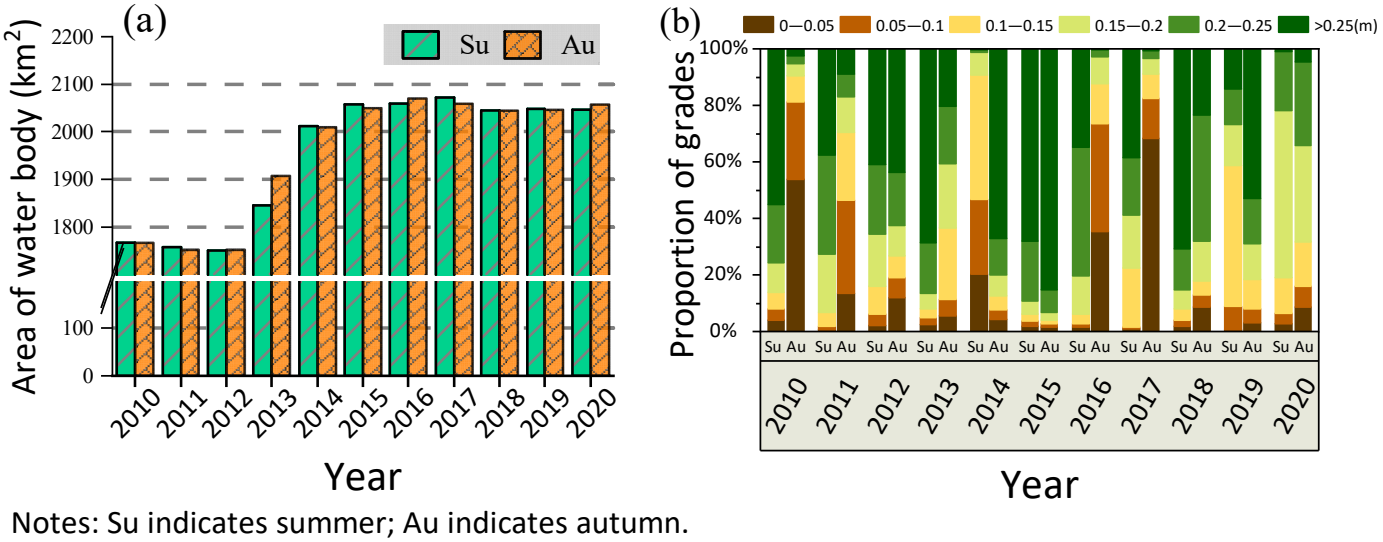

Figure 6. Statistical values of the area, including (**a**) area of the water body; (**b**) proportion of grades.

3.1.2. Spatial Pattern of Transparency

The spatial pattern of the multiyear SDD in the Hulun Lake is shown in Figure 7 (summer) and 7 (autumn). The bottom left corner of each graph shows the SDE distribution of SDD. The SDE_max (or SDE_min) represents the SDE of values greater (or less) than the mean SDD value, and the MCen_max (or MCen_min) represents the MCen of values greater (or less) than the mean SDD value. From northeast to southwest, the transparency parameter of Hulun Lake showed significant variations. Overall, the SDD values were lower in the north-eastern part of Hulun Lake than in the south-western part. In addition, the SDD values showed evident seasonal change (see Table A2). From 2010 to 2020, Hulun Lake had high SDD values in summer, with uniform distribution of the pixels with high SDD values (>mean) and the pixels with low SDD values (<mean) (Figure 7). Compared to the position of MCen_max, MCen_min was closer to the northeastern part of Hulun Lake. Except for a few years, compared with SDE_max, SDE_min had a longer long axis and larger area. The SDD values in the northeastern part of Hulun Lake were slightly less than those in the south-western part, with higher SDD values near the upper part of the Klulun River and near the Urxun River than near the lower part of the Klulun River.

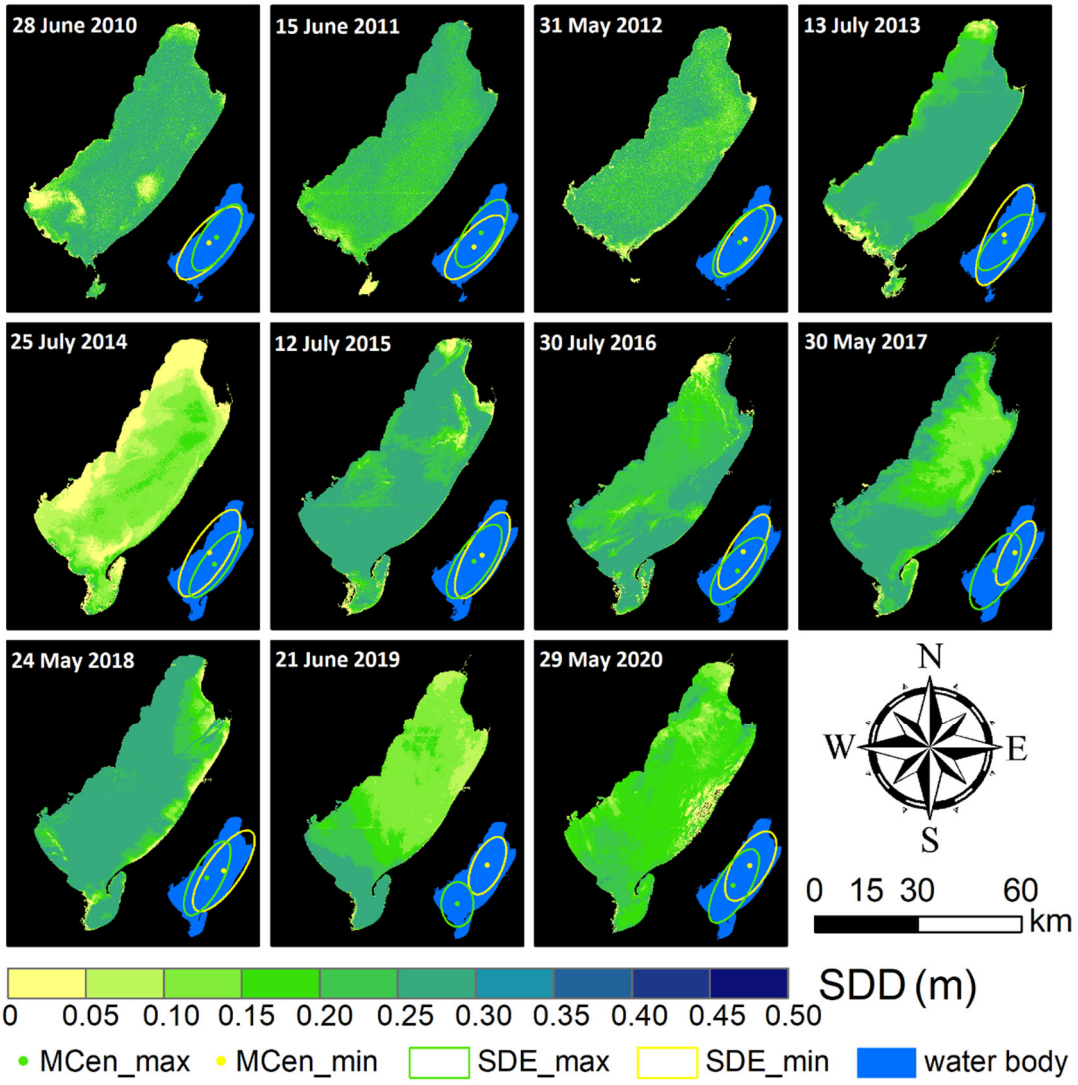

Figure 7. Spatial pattern of summer transparency in Hulun Lake from 2010 to 2020. The lower right corner is the spatial distribution of the standard deviation ellipse and the mean center of the transparency, the blue background represents the current water body range, the green represents the SDD values (>mean), and the yellow represents the SDD values (<mean).

In autumn, the SDD values of Hulun Lake decreased, with an obvious difference in the distribution between the pixels with high SDD values (>mean) and pixels with low SDD values (<mean) (Figure 8). Compared to the position of MCen_min, MCen_max was closer to the western part of Hulun Lake. The SDD values around Hulun Lake were significantly lower than in the center. Similar results can be derived by analyzing the distribution of SDE. In contrast to SDE_max, SDE_min had a longer short axis, a longer long axis, and a larger area. In addition, pixel-scale trend analysis and testing showed significant seasonal differences in SDD over the study period, confirming that transparency is closely related to climatic factors and geographical location.

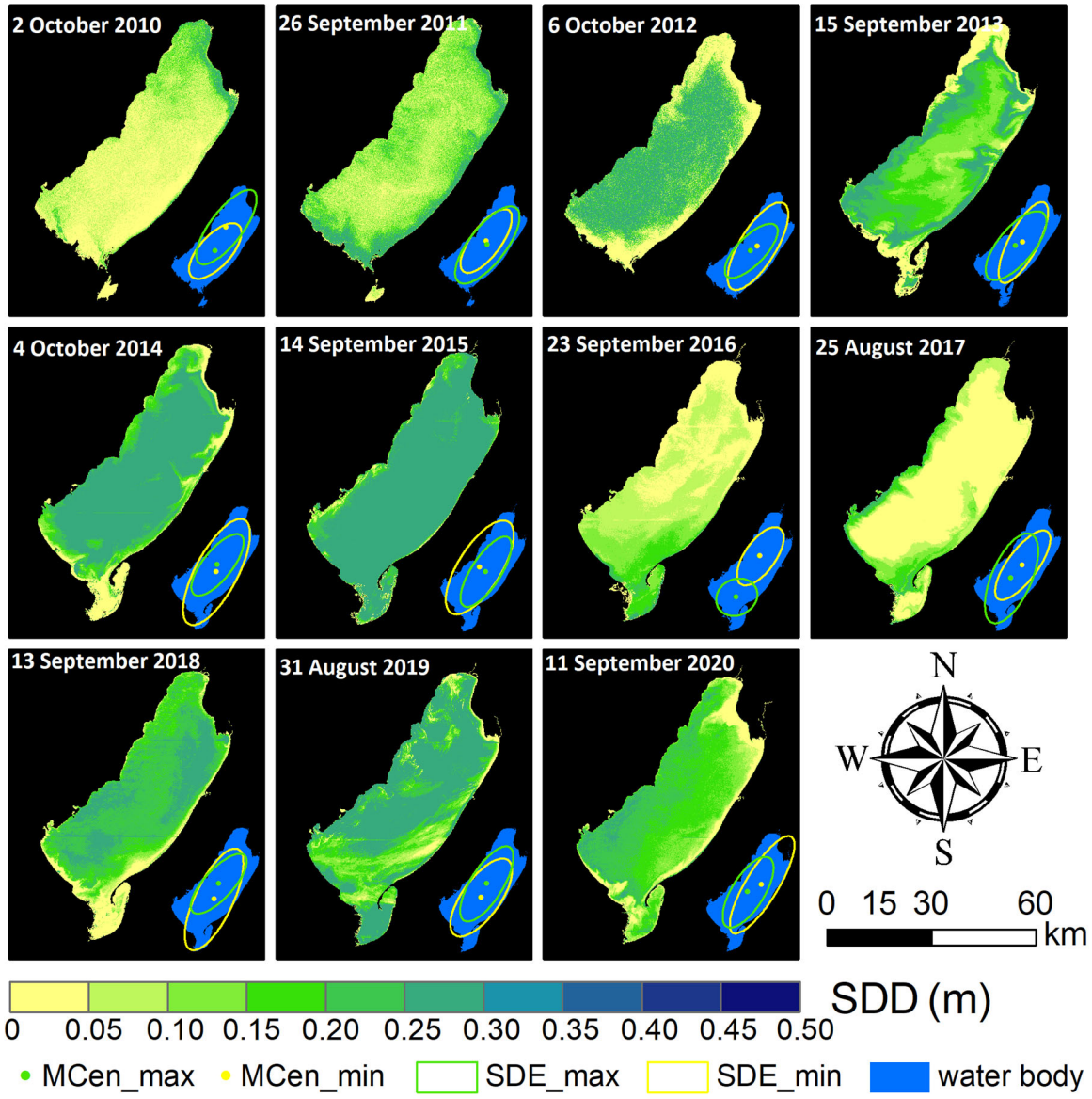

Figure 8. Spatial pattern of autumn transparency in Hulun Lake from 2010 to 2020. The lower right corner is the spatial distribution of the standard deviation ellipse and the mean center of the transparency, the blue background represents the current water body range, the green represents the SDD values (>mean), and the yellow represents the SDD values (<mean).

3.2. Drivers of Transparency Variation

3.2.1. Climate Factors

In this paper, the meteorological station data for Hulun Lake, including temperature, precipitation, and wind speed, were obtained from 2010 to 2020 (Figure 9). The peak

temperature of Hulun Lake occurs in July each year, with the highest temperature around 28 °C and the temperature below 0 °C from late October to early April of the following year. Rainfall was mainly concentrated from June to August each year. There was an increasing rainfall trend after 2010, with an annual cumulative rainfall of 401.57 mm and 503.68 mm in 2014 and 2020, respectively. Overall, the wind speed was approximately 7 m/s from 2010 to 2014 and increased to approximately 10 m/s after 2014. In summer, sudden decreases and increases in SDD were observed in 2014 and 2015, respectively. The annual average temperature in 2014 was low, with a maximum temperature of 21 °C during the year. During the study period, the average daily wind speed was about 14 m/s, and the cumulative rainfall for a week was 24.13 mm. In 2015, the temperature during the study period reached the highest annual temperature, the cumulative rainfall for a week was 0 mm, and the average daily wind speed was 6 m/s. In autumn, sudden decreases and increases in SDD occurred in 2016 and 2018, respectively. In 2016, the cumulative rainfall for one week was 2.03 mm, and the average daily wind speed was about 14 m/s. In 2018, the temperature during the study period reached about 14 °C, the cumulative rainfall for one week was 6.10 mm, and the average daily wind speed was 10 m/s. In general, although there was no obvious pattern of temperature and SDD variation, the occurrence of low SDD was always accompanied by frequent rainfall and strong winds (see Table A3). This confirms that the variation of SDD is significantly related to precipitation and wind speed, which is consistent with the findings of previous research [9]. In summer, the Pearson correlation coefficient (R) between one-week cumulative precipitation and SDD was −0.39. In autumn, the Pearson correlation coefficient (R) between SDD and one-week cumulative precipitation and wind speed was 0.37 and −0.40, respectively.

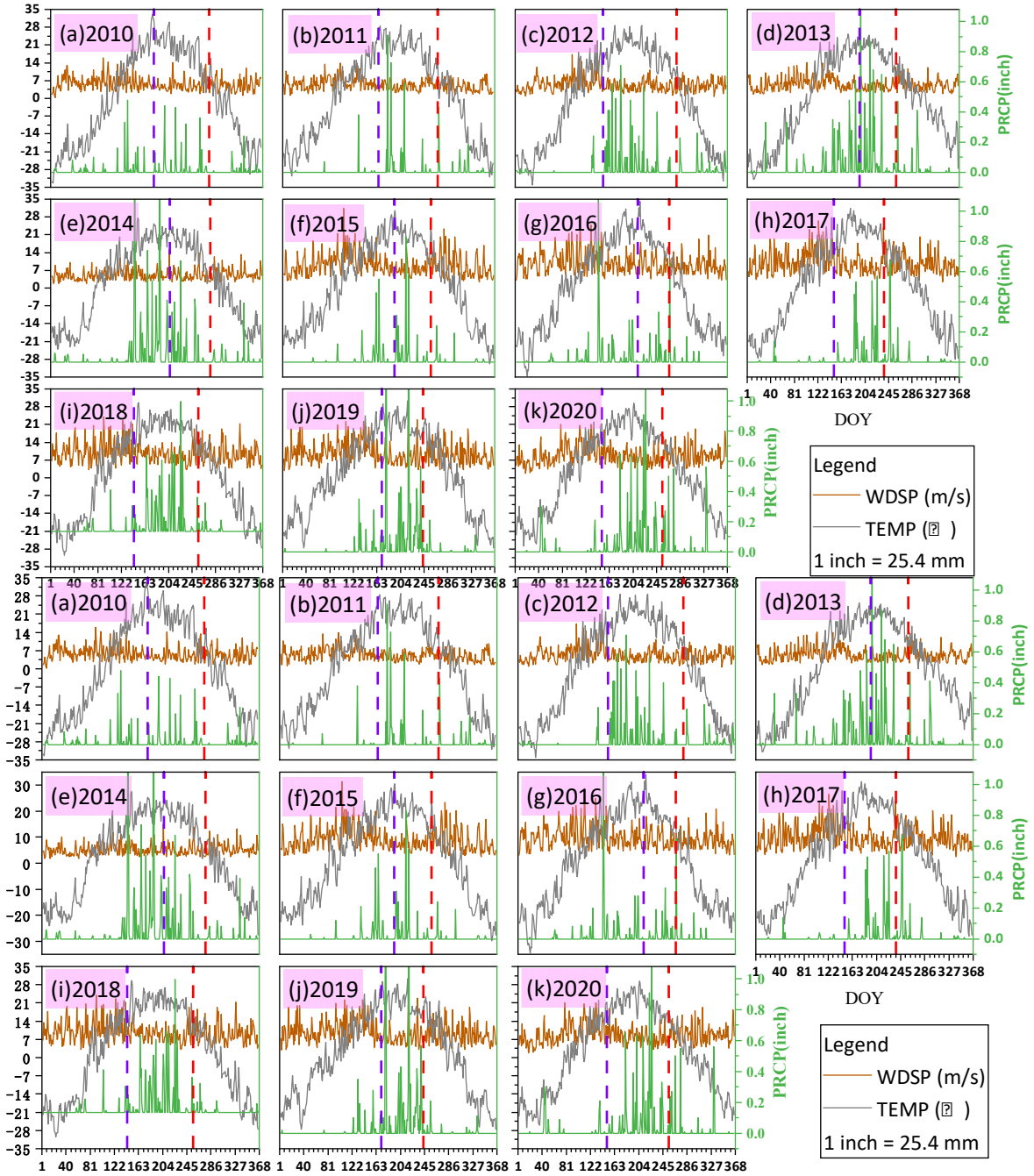

Figure 9. Parameters of climate factors in the Hulun Lake from 2010 to 2020. The blue and red dotted lines in each coordinate system represent the transparency inversion dates for summer and autumn of the corresponding year, respectively.

3.2.2. Human Activities

From a global perspective, record-breaking harmful algal blooms and other severe water quality events have become more frequent in recent decades due to human activities [50]. For example, urban expansion has led to more intensive human activity, contributing to the trophication of inland water bodies [51]. In addition, local agricultural practices (e.g., cropland irrigation, winter fishing) can also cause changes in water quality [52,53]. In 2010, the area of vegetation (the sum of grassland and sparse vegetation), cropland, and the impervious surface were 27137.9 km^2, 87.5 km^2, and 198.5 km^2, respectively. Cropland has expanded significantly, and the area of cropland in 2015 increased to

350.9 km². Since then, the area of vegetation continued to degrade, and cropland and impervious surface continued to expand, with the area of vegetation, cropland, and impervious surface in 2020 being 26,320.2 km², 574.9 km², and 272.3 km², respectively (see Figure 10). In the past ten years, the vegetation coverage area around Hulun Lake has decreased by 817.8 km², and the area of the cropland and the impervious surface has increased by 487.5 km² and 47.8 km², respectively. The cropland and impervious surface were mainly distributed in the northeast and southwest of Hulun Lake. The cropland area in the Klulun river basin has increased significantly, which may be the main reason for the lower SDD at the entrance of Hulun Lake. Land use and land cover have been considered as potential indirect drivers of spatial and temporal variability in transparency [54].

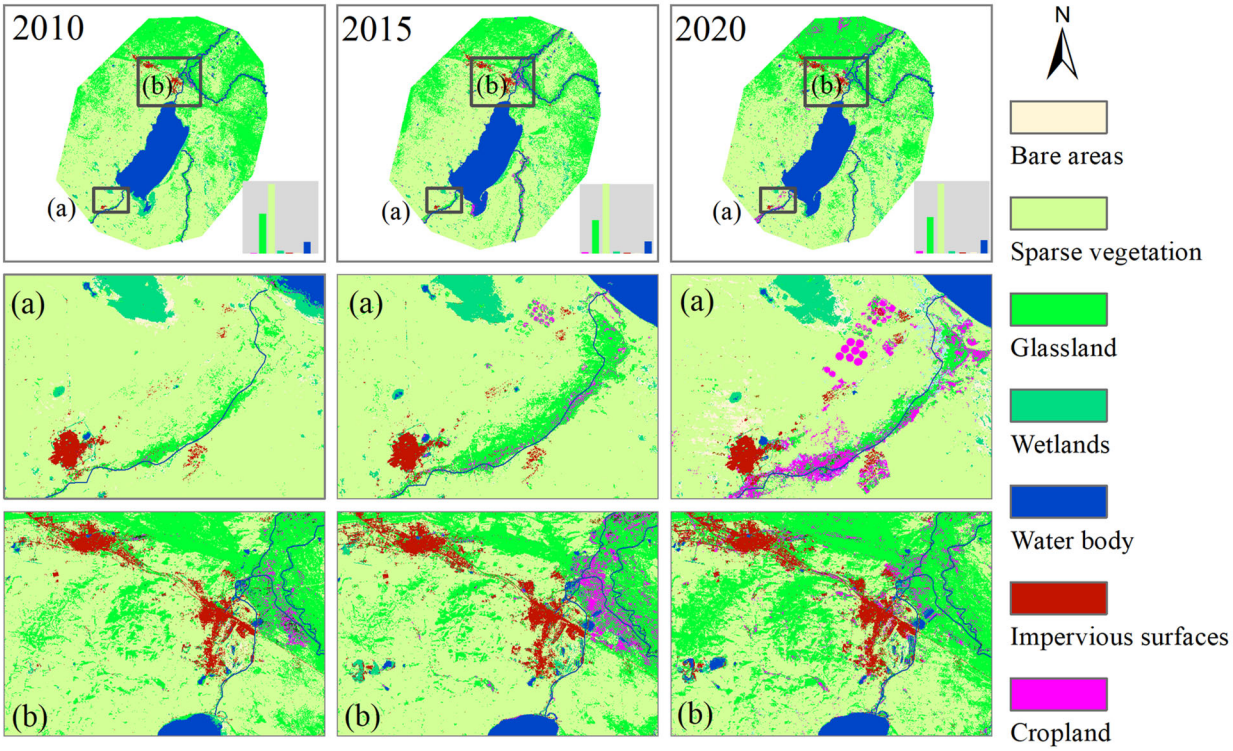

Figure 10. Land use/land cover images of Hulun Lake from 2010 to 2020. (**a**) Land use/land cover in the southwest of the study area; (**b**) Land use/land cover in the northeast of the study area.

4. Discussion

4.1. Transparency Characteristics of Hulun Lake

The great value of Hulun Lake in maintaining natural habitats and protecting biodiversity has been recognized by many researchers [22–24,27]. However, Hulun Lake has serious eutrophication and poor water quality. Our results confirmed that the water transparency of Hulun Lake has been low since 2010, the SDD in summer was higher than that in autumn, and the maximum SDD was less than 0.3 m, which is consistent with the research conclusions of Wang et al. [55]. In addition, there were obvious spatial characteristics in the SDD of Hulun Lake. Specifically, there was a significant difference in SDD between the entrance and exit of the lake in summer (i.e., the transparency is greater at the lake entrance than at the exit), and an evident difference in SDD between the littoral zones and central parts of the lake in autumn (i.e., the transparency is greater at the lake's central parts than at the littoral zones). As a positive response to the declining water quality of Hulun Lake, the government has taken a series of measures. For example, the "diversion from river to lake" project and the "river-lake connection" project were implemented in 2009; the "lake closure" policy was implemented in 2013, and the "one lake-two seas" ecological protection project was implemented in 2019. The protective measures

implemented by the government have had a positive effect on limiting the continued decline in water quality in Hulun Lake. Although Landsat imagery can provide 30 m spatial resolution on the earth's surface, due to the complex background of water bodies, the imagery still cannot accurately identify the in-situ measured characteristics. Considering the deficiencies of Landsat imagery, joint daytime high-resolution optical observation for feature identification is a feasible solution. For example, fusing Gaofen satellite data or Sentinel-2 MSI data to generate high spatial resolution images to reduce the difference in "point-to-surface" conversion.

4.2. Uncertainty of Transparency Inversion Model

Due to the limited number of measured points, there are the following two theoretical uncertainties: (1) spatial uncertainty and, theoretically, there is uncertainty in predicting the transparency of water bodies in the southern and eastern parts of Hulun Lake using the measured points distributed in the northern and western parts of the lake; (2) temporal uncertainty. In this paper, we use the measured points collected in summer (July), so there is theoretical uncertainty in predicting the transparency of Hulun Lake in autumn. Cheng et al. pointed out that the spatial variability of water quality parameters in inland lakes may be both structural and random, but the spatial heterogeneity is more derived from structural factors than random factors [56]. That is to say, except for the outlet and inlet of Hulun Lake, it is feasible to predict the transparency of the entire lake using the measurement points distributed in the northern and western parts of Hulun Lake. In addition, we found that the Pearson correlation coefficient between precipitation and SDD in summer (−0.39) and autumn (0.37) was less than 0.5. Statistics show that the difference in climate conditions between summer and autumn is not obvious, and both have the characteristics of more precipitation and fast wind speed. Therefore, it is feasible to predict the autumn transparency of Hulun Lake using the model constructed from the summer data.

There are three approaches to inversion methods for SDD, including analytical, semi-analytical, and empirical algorithms. In analytical algorithms, satellite images are preprocessed to achieve accurate atmospheric correction using the corresponding radiative transfer models. The analytical methods require rigorous theoretical derivation and are challenging because instantaneous atmospheric conditions and initial parameter values are difficult to acquire [54,57]. In semi-analytical algorithms, hyperspectral scanner data from field observations, on-board imagery, and satellite hyperspectral imagery are typically applied to establish the reflectance curve of the studied water body. The spectral bands corresponding to the SDD value are then determined according to the characteristics of the reflectance curve [57]. The most commonly used semi-analytical methods involve deriving the absorption and backscattering coefficients of water substances (such as COD, TP, and DO) from the water surface reflectance [54,57,58]. These derived parameters are then used to calculate other related parameters such as turbidity and total suspended matter concentration (TSM). Semi-analytical methods have complex parameterization processes and high spectral resolution requirements for satellite images, which severely limit their application for deriving water transparency [58]. According to reports, the optical properties of inland waters are often complex, which makes it rather challenging for analytical and semi-analytical algorithms to derive SDD directly from the remote sensing reflectance [10]. In the empirical algorithm, the regression relationship between band reflectance and field measured transparency values are used for the SDD inversion. The empirical methods have been successfully used in specific regions [5,10]. Therefore, we used empirical algorithms to develop the remote sensing algorithms for SDD. Two main aspects were considered when building the model. (1) all single-bands and band-combinations (i.e., the number of bands is less than or equal to (3) were tested (N = 237) to obtain the most sensitive factor for SDD in the study area; (2) 100 sample points were selected for model accuracy validation within the buffer zone established by the actual measurement points to select the best inversion model for SDD in the study area. The above

methods have proven to be accurate for SDD inversion when the number of sample points is not sufficient. In addition, machine learning (ML) and deep learning (DL) algorithms have the ability to automatically learn spectral parameter features and can establish nonlinear models for transparency inversion [45,59]. If supported by sufficient sample data, ML and DL algorithms will be used in the next research.

4.3. Further Research

In this paper, we conducted a long-term remote sensing monitoring study of the transparency of Hulun Lake. Although the results of the study contribute to the understanding of the spatio-temporal patterns and drivers of transparency, there are still some aspects that deserve to be further understood and improved. First, in order to achieve long-term transparency monitoring, we combined the spectral data from three sensors (TM, ETM+, and OLS). Although the linear regression model was used for spectral correction [30,31], there are still uncertain spectral spots. Therefore, data continuity correction should be carried out under the background of low radiation to obtain more accurate and consistent transparency monitoring. Secondly, Xu pointed out that an appropriate increase of the MNDWI threshold (>0) can effectively reduce the influence of buildings and shadows and achieve a better extraction effect of the water body range [37,39]. It was confirmed by experimental cases in Lakes Dire and Legedadi in Ethiopia that the accuracy is higher for thresholds greater than 0 (approximately 0.1) when using MNDWI for water extraction in turbid lakes [40]. Although the MNDWI index was widely used to extract the water body area, there is still a non-negligible error using a threshold method. In addition, the impact of climate change on water quality parameters is very obvious [14,60–62]. Temperature increases (or decreases) can accelerate (or inhibit) the growth of phytoplankton in the water, thus changing the chlorophyll content, transparency, and other parameters. The effect of precipitation on the parameters is also significant. On the one hand, surface runoff caused by precipitation accelerates sediment transfer into the water. On the other hand, precipitation makes suspended solids in the water no longer precipitate. In addition, wind speed is also a driving factor for changes in water quality parameters [9,63]. Therefore, exploring the relationship between climatic factors and the transparency of Hulun Lake can help us better optimize lake planning strategies to protect the ecological health of the basin. Although the driving effects of climate factors and human activities on the water quality changes in Hulun Lake were discussed in detail, there is no quantitative description of the two types of driving factors. This motivates us to use more powerful statistical analysis models (e.g., the Geographical Detector Model) for quantitative research [64] on driving factors in future research.

5. Conclusions

This paper used the satellite-derived method to extract the transparency of Hulun Lake and further analyzed its spatial and temporal dynamics. In addition, the driving factors of transparency were also explored.

(1) Based on in situ measured data, we found that B3/(B1 + B4) [red/(blue-NIR)] was the most sensitive parameter for transparency (R = 0.84) and the exponential model was the most suitable SDD satellite algorithm for Hulun Lake (R^2 = 0.665, RMSE = 0.055 m, MAE = 0.003 m);
(2) During the study period, the annual mean SDD of Lake Hulun was higher in summer than in autumn. There were fluctuations in SDD in both summer and autumn, indicating that SDD was influenced by climatic and anthropogenic factors. The SDD showed a decreasing trend in summer (−0.035 m/decade) and an increasing trend in autumn (0.052 m/decade). In the littoral zones of Hulun Lake, SDD was lower than in the central region. In addition, the SDD in the northeastern part of Hulun Lake was lower than that in the southwestern part;
(3) Precipitation and wind speed were highly correlated with changes in SDD, particularly cumulative precipitation and mean wind speed over a week (starting at the time

of image acquisition). In contrast, the relationship between temperature and SDD variation was not significant. In addition, the expansion of cropland and impervious surfaces in the Klulun River basin was the possible cause of the low SDD at the entrance to the Hulun Lake flow.

Author Contributions: Conceptualization, Y.Z. and W.G.; methodology, C.Z.; software, C.Z. and W.G.; validation, Y.Z., W.G., and M.F.B.; formal analysis, C.Z. and W.G.; investigation, C.Z. and Y.Z.; resources, W.G. and C.Z.; data curation, C.Z.; writing—original draft preparation, C.Z. and W.G.; writing—review and editing, M.F.B., W.G., and Y.Z.; visualization, Y.Z. and C.Z.; supervision, W.G. and Y.Z.; project administration, Y.Z.; funding acquisition, Y.Z. All authors have read and agreed to the published version of the manuscript.

Funding: This research was funded by the Major Projects of High-Resolution Earth Observation Systems of National Science and Technology(05-Y30B01-9001-19/20-3); the State Key Laboratory of Geo-Information Engineering and Key Laboratory of Surveying and Mapping Science and Geospatial Information Technology of MNR, CASM (2021-03-04); the National Natural Science Foundation of China (Grant No. 41971324).

Institutional Review Board Statement: Not applicable.

Informed Consent Statement: Not applicable.

Data Availability Statement: The data presented in this study are available on request from the corresponding author.

Acknowledgments: The authors would like to acknowledge Lake-Watershed Science Data Center, National Earth System Science Data Sharing Infrastructure, National Science & Technology Infrastructure of China (http://lake.geodata.cn, accessed on 7 May 2021) for providing ground observed SDD data. The authors are grateful for the comments from anonymous reviewers and the editors.

Conflicts of Interest: The authors declare no conflict of interest.

Appendix A

Table A1. Sensitivity testing (N = 237) between bands and SDD.

Band	R	Band	R	Band	R	Band	R	Band	R
B1	−0.53	lnB2 − lnB4	0.40	B3/(B3 + B4)	0.61	B6/(B4 + B5)	0.59	b4 * (b2 − b5)/(b2 * b5)	−0.59
B2	−0.717 *	lnB2 − lnB5	−0.32	B3/(B3 + B5)	0.41	B6/(B4 + B6)	0.44	b6 * (b2 − b5)/(b2 * b5)	−0.55
B3	−0.26	lnB2 − lnB6	−0.18	B3/(B3 + B6)	0.00	B6/(B5 + B6)	0.43	b1 * (b2 − b6)/(b2 * b6)	−0.12
B4	−0.675 *	lnB3 − lnB4	0.60	B3/(B4 + B5)	0.769 *	b1 − b2	0.35	b3 * (b2 − b6)/(b2 * b6)	0.02
B5	−0.41	lnB3 − lnB5	−0.16	B3/(B4 + B6)	0.48	b1 − b3	−0.61	b4 * (b2 − b6)/(b2 * b6)	−0.11
B6	−0.12	lnB3 − lnB6	0.02	B3/(B5 + B6)	0.44	b1 − b4	−0.01	b5 * (b2 − b6)/(b2 * b6)	−0.33
B1/B2	−0.18	lnB4 − lnB5	−0.46	B4/(B1 + B2)	−0.33	b1 − b5	−0.33	b1 * (b3 − b4)/(b3 * b4)	0.36
B1/B3	−0.62	lnB4 − lnB6	−0.42	B4/(B1 + B3)	−0.46	b1 − b6	−0.49	b2 * (b3 − b4)/(b3 * b4)	0.50
B1/B4	0.17	lnB5 − lnB6	0.36	B4/(B1 + B4)	−0.18	b2 − b3	−0.728 *	b5 * (b3 − b4)/(b3 * b4)	−0.12
B1/B5	−0.55	B1/(B1 + B2)	−0.17	B4/(B1 + B5)	−0.02	b2 − b4	−0.33	b6 * (b3 − b4)/(b3 * b4)	0.62
B1/B6	−0.12	B1/(B1 + B3)	−0.63	B4/(B1 + B6)	−0.28	b2 − b5	−0.49	b1 * (b3 − b5)/(b3 * b5)	−0.55
B2/B3	0.667 *	B1/(B1 + B4)	0.18	B4/(B2 + B3)	−0.54	b2 − b6	−0.694 *	b2 * (b3 − b5)/(b3 * b5)	−0.55
B2/B4	0.37	B1/(B1 + B5)	0.35	B4/(B2 + B4)	−0.41	b3 − b4	0.41	b4 * (b3 − b5)/(b3 * b5)	−0.59
B2/B5	−0.56	B1/(B1 + B6)	−0.27	B4/(B2 + B5)	−0.25	b3 − b5	0.00	b6 * (b3 − b5)/(b3 * b5)	−0.54
B2/B6	−0.11	B1/(B2 + B3)	−0.42	B4/(B2 + B6)	−0.48	b3 − b6	−0.23	b1 * (b3 − b6)/(b3 * b6)	−0.10
B3/B4	0.58	B1/(B2 + B4)	0.00	B4/(B3 + B4)	−0.61	b4 − b5	−0.34	b2 * (b3 − b6)/(b3 * b6)	−0.10
B3/B5	−0.53	B1/(B2 + B5)	0.01	B4/(B3 + B5)	−0.43	b4 − b6	−0.698 *	b4 * (b3 − b6)/(b3 * b6)	−0.36
B3/B6	0.04	B1/(B2 + B6)	−0.18	B4/(B3 + B6)	−0.65	b5 − b6	−0.36	b5 * (b3 − b6)/(b3 * b6)	−0.32
B4/B5	−0.59	B1/(B3 + B4)	−0.28	B4/(B4 + B5)	0.29	b3 * (b1 − b2)/(b1 * b2)	−0.39	b1 * (b4 − b5)/(b4 * b5)	−0.56
B4/B6	−0.40	B1/(B3 + B5)	−0.42	B4/(B4 + B6)	−0.44	b4 * (b1 − b2)/(b1 * b2)	0.02	b2 * (b4 − b5)/(b4 * b5)	−0.56
B5/B6	−0.33	B1/(B3 + B6)	−0.58	B4/(B5 + B6)	0.22	b5 * (b1 − b2)/(b1 * b2)	0.33	b3 * (b4 − b5)/(b4 * b5)	−0.54
B2/B1	0.19	B1/(B4 + B5)	0.37	B5/(B1 + B2)	0.09	b6 * (b1 − b2)/(b1 * b2)	−0.28	b6 * (b4 − b5)/(b4 * b5)	−0.55
B3/B1	0.63	B1/(B4 + B6)	0.09	B5/(B1 + B3)	0.15	b2 * (b1 − b3)/(b1 * b3)	−0.58	b1 * (b4 − b6)/(b4 * b6)	−0.15
B4/B1	−0.20	B1/(B5 + B6)	0.31	B5/(B1 + B4)	0.08	b4 * (b1 − b3)/(b1 * b3)	−0.40	b2 * (b4 − b6)/(b4 * b6)	−0.15
B5/B1	−0.33	B2/(B1 + B2)	0.17	B5/(B1 + B5)	0.06	b5 * (b1 − b3)/(b1 * b3)	0.12	b3 * (b4 − b6)/(b4 * b6)	−0.03
B6/B1	0.28	B2/(B1 + B3)	−0.34	B5/(B1 + B6)	0.09	b6 * (b1 − b3)/(b1 * b3)	−0.52	b4 * (b4 − b6)/(b4 * b6)	−0.40
B3/B2	0.64	B2/(B1 + B4)	0.56	B5/(B2 + B3)	0.12	b2 * (b1 − b4)/(b1 * b4)	0.22	b1 * (b5 − b6)/(b5 * b6)	0.57
B4/B2	−0.43	B2/(B1 + B5)	0.34	B5/(B2 + B4)	0.07	b3 * (b1 − b4)/(b1 * b4)	0.30	b2 * (b5 − b6)/(b5 * b6)	0.56
B5/B2	−0.32	B2/(B1 + B6)	0.11	B5/(B2 + B5)	0.05	b5 * (b1 − b4)/(b1 * b4)	−0.11	b3 * (b5 − b6)/(b5 * b6)	0.56
B6/B2	0.24	B2/(B2 + B3)	−0.66	B5/(B2 + B6)	0.07	b6 * (b1 − b4)/(b1 * b4)	0.34	b4 * (b5 − b6)/(b5 * b6)	0.57
B4/B3	−0.63	B2/(B2 + B4)	0.41	B5/(B3 + B4)	0.15	b2 * (b1 − b5)/(b1 * b5)	−0.56	(b1 − b2)/(B1 + B2)	−0.17
B5/B3	−0.40	B2/(B2 + B5)	0.34	B5/(B3 + B5)	0.14	b3 * (b1 − b5)/(b1 * b5)	−0.54	(b1 − b3)/(B1 + B3)	−0.63
B6/B3	0.01	B2/(B2 + B6)	−0.22	B5/(B3 + B6)	0.17	b4 * (b1 − b5)/(b1 * b5)	−0.59	(b1 − b4)/(B1 + B4)	0.18
B5/B4	−0.25	B2/(B3 + B4)	−0.31	B5/(B4 + B5)	0.00	b6 * (b1 − b5)/(b1 * b5)	−0.55	(b1 − b5)/(B1 + B5)	0.35
B6/B4	0.44	B2/(B3 + B5)	−0.27	B5/(B4 + B6)	0.05	b2 * (b1 − b6)/(b1 * b6)	−0.12	(b1 − b6)/(B1 + B6)	−0.26
B6/B5	−0.55	B2/(B3 + B6)	−0.667 *	B5/(B5 + B6)	−0.09	b3 * (b1 − b6)/(b1 * b6)	0.01	(b2 − b3)/(B2 + B3)	−0.65
ln(B1)	−0.54	B2/(B4 + B5)	0.60	B6/(B1 + B2)	0.26	b4 * (b1 − b6)/(b1 * b6)	−0.37	(b2 − b4)/(B2 + B4)	0.41
ln(B2)	−0.714 *	B2/(B4 + B6)	0.23	B6/(B1 + B3)	0.13	b5 * (b1 − b6)/(b1 * b6)	−0.33	(b2 − b5)/(B2 + B5)	0.34
ln(B3)	−0.25	B2/(B5 + B6)	0.35	B6/(B1 + B4)	0.34	b1 * (b2 − b3)/(b2 * b3)	−0.710 *	(b2 − b6)/(B2 + B6)	−0.24
ln(B4)	−0.66	B3/(B1 + B2)	0.728 *	B6/(B1 + B5)	0.37	b4 * (b2 − b3)/(b2 * b3)	−0.710 *	(b3 − b4)/(B3 + B4)	0.61
ln(B5)	0.18	B3/(B1 + B3)	0.63	B6/(B1 + B6)	0.27	b5 * (b2 − b3)/(b2 * b3)	−0.64	(b3 − b5)/(B3 + B5)	0.41
ln(B6)	−0.11	B3/(B1 + B4)	0.841 **	B6/(B2 + B3)	0.13	b6 * (b2 − b3)/(b2 * b3)	−0.58	(b3 − b6)/(B3 + B6)	−0.01
lnB1 − lnB2	−0.17	B3/(B1 + B5)	0.64	B6/(B2 + B4)	0.33	b1 * (b2 − b4)/(b2 * b4)	0.23	(b4 − b5)/(B4 + B5)	0.28
lnB1 − lnB3	−0.64	B3/(B1 + B6)	0.692 *	B6/(B2 + B5)	0.33	b3 * (b2 − b4)/(b2 * b4)	0.52	(b4 − b6)/(B4 + B6)	−0.43
lnB1 − lnB4	0.18	B3/(B2 + B3)	0.66	B6/(B2 + B6)	0.22	b5 * (b2 − b4)/(b2 * b4)	−0.20	(b5 − b6)/(B5 + B6)	−0.43
lnB1 − lnB5	−0.27	B3/(B2 + B4)	0.672 *	B6/(B3 + B4)	0.15	b6 * (b2 − b4)/(b2 * b4)	0.52		
lnB1 − lnB6	−0.20	B3/(B2 + B5)	0.745 *	B6/(B3 + B5)	0.15	b1 * (b2 − b5)/(b2 * b5)	−0.55		
lnB2 − lnB3	−0.65	B3/(B2 + B6)	0.61	B6/(B3 + B6)	0.00	b3 * (b2 − b5)/(b2 * b5)	−0.54		

(*): significant correlation for $p < 0.05$. (**): significant correlation for $p < 0.01$

Table A2. SDE parameters of transparency.

Season	Summer						Autumn					
SDE parameters	SDE_max			SDE_min			SDE_max			SDE_min		
	La(m)	Sa(m)	MCen_max	La(m)	Sa(m)	MCen_min	La(m)	Sa(m)	MCen_max	La(m)	Sa(m)	MCen_min
2010	26,226.3	10,048.7	(117.44,48.99)	30,703.8	12,195.4	(117.36,48.96)	30,006.7	10,883.9	(117.48,49.08)	23,159.5	10,455.3	(117.38,48.93)
2011	26,662.2	10,871.6	(117.44,49.02)	27,567.4	10,621.4	(117.37,48.93)	31,164.1	12,098	(117.42,48.97)	25,350.6	9924.6	(117.41,48.99)
2012	27,465.7	10,765	(117.39,48.98)	28,150.7	11,007.9	(117.45,48.99)	23,438.9	9316	(117.39,48.97)	33,272.2	12,118.9	(117.45,49.00)
2013	25,227.4	9445.9	(117.41,48.96)	37,808.8	12,291.1	(117.41,49.00)	28,764.6	11,942.9	(117.37,48.95)	30,586.2	9860.3	(117.44,48.97)

2014	27,143.6	8937.9	(117.42,48.92)	34,571	12,218.7	(117.37,49.00)	25,636.7	9873.2	(117.40,48.97)	40,165.3	14,343.8	(117.39,48.93)
2015	29,653.4	11,603.5	(117.38,48.94)	33,184.4	11,793.4	(117.45,48.98)	28,702.3	10,298.4	(117.41,48.95)	37,794.1	15,095.7	(117.35,48.98)
2016	28,542.6	12,137.6	(117.38,48.90)	30,551.6	10,317.3	(117.43,49.03)	15,041.5	12,699.4	(117.25,48.79)	24,103.5	10,860.5	(117.48,49.05)
2017	30,149.1	12,722.8	(117.31,48.90)	25,505.9	8891.6	(117.51,49.02)	33,220.4	13,654.3	(117.33,48.90)	28,628.7	10,405.2	(117.43,48.98)
2018	28,728.7	10,353.7	(117.36,48.94)	33,495.1	11,987.1	(117.51,48.97)	26,063.6	9864.7	(117.41,48.98)	37,805.1	12,848.9	(117.37,48.89)
2019	16,006.2	11,509.5	(117.21,48.80)	22,158.6	10,537.8	(117.51,49.04)	29,331.4	11,011.9	(117.42,48.98)	31,270.5	12,884.2	(117.37,48.90)
2020	28,941.4	11,176.2	(117.34,48.90)	27,361.9	12,387.9	(117.50,49.03)	28,881.3	11,585.7	(117.38,48.95)	40,184.2	11,445.4	(117.52,48.99)

Table A3. Meteorological station data of Hulun Lake.

		TEMP (°C)				PRCP (inch)				WDSP (m/s)			
		Three-Day	One-Week	One-Month	Two-Month	One-Day	Three-Day	One-Week	Two-Week	One-Day	Three-Day	One-Week	Two-Week
2010	Su	32.22	28.93	22.42	17.80	0.00	0.00	0.00	0.00	5.00	5.07	4.80	5.54
	Au	7.15	5.97	13.36	16.14	0.00	0.00	0.10	0.25	6.30	5.40	7.56	7.14
2011	Su	23.46	20.91	16.38	12.90	0.00	0.00	0.01	0.02	5.10	4.70	4.90	4.98
	Au	13.46	12.90	13.64	17.72	0.00	0.00	0.00	0.04	3.90	5.93	5.04	5.33
2012	Su	12.80	15.34	13.66	9.05	0.00	0.00	0.00	0.00	2.70	5.67	5.31	8.03
	Au	9.61	10.48	13.56	15.74	0.00	0.00	0.00	0.18	1.70	5.17	3.57	4.73
2013	Su	22.06	21.26	20.55	18.08	0.00	0.18	0.96	1.39	2.70	3.30	3.40	4.53
	Au	10.09	11.74	15.40	18.46	0.02	0.10	0.16	0.17	12.40	7.80	7.07	5.58
2014	Su	20.96	20.60	20.75	20.09	0.00	0.06	0.95	0.95	3.20	4.47	5.07	4.64
	Au	5.59	4.60	11.63	15.06	0.00	0.00	0.00	0.05	2.50	2.70	4.14	4.18
2015	Su	23.93	26.22	22.02	18.63	0.00	0.00	0.00	0.02	5.10	6.00	7.19	7.27
	Au	13.83	12.75	17.85	19.78	0.00	0.00	0.08	0.15	5.60	8.60	9.94	8.81
2016	Su	24.37	22.69	24.75	22.00	0.00	0.01	0.01	0.71	5.10	5.50	8.56	9.03
	Au	15.15	13.65	16.04	19.81	0.00	0.00	0.08	0.23	4.90	7.73	7.71	7.78
2017	Su	14.70	17.42	14.63	10.63	0.00	0.00	0.00	0.00	17.00	17.97	13.59	13.28
	Au	15.67	19.60	21.78	23.34	0.00	0.02	0.03	0.69	23.80	15.13	11.83	9.69
2018	Su	11.85	16.61	14.09	9.23	0.00	0.30	0.30	0.40	10.90	15.80	11.80	12.28
	Au	16.17	13.43	18.24	20.21	0.00	0.24	0.24	0.31	12.60	10.43	10.83	10.99
2019	Su	24.69	22.02	18.70	14.62	0.12	0.22	0.22	0.58	5.80	7.30	7.49	8.21
	Au	17.15	16.91	18.51	20.40	0.06	0.34	1.11	2.46	5.80	7.60	7.59	9.20
2020	Su	19.19	16.23	14.59	9.97	0.00	0.00	0.01	0.37	12.40	8.27	10.96	9.96
	Au	16.72	16.20	17.23	19.95	0.05	0.05	0.05	0.98	5.80	6.90	7.64	7.07

Note: In the table, TEMP and WDSP were calculated using the average of the time periods; PRCP was calculated using the sum of the time periods; 1 inch = 25.4 mm.

References

1. Tao, S.; Fang, J.; Ma, S.; Cai, Q.; Xiong, X.; Tian, D.; Zhao, X.; Fang, L.; Zhang, H.; Zhu, J.; et al. Changes in China's lakes: Climate and human impacts. *Natl. Sci. Rev.* **2020**, *7*, 132–140.
2. Liu, J.; Yang, W. Water sustainability for China and beyond. *Science* **2012**, *337*, 649–650.
3. Ma, T.; Zhao, N.; Ni, Y.; Yi, J.P.; Wilson, J.; He, L.; Du, Y.; Pei, T.; Zhou, C.; Song, C.; et al. China's improving inland surface water quality since 2003. *Sci. Adv.* **2021**, *6*, 3798–3807.
4. Bao, L.; Maruya, K.A.; Snyder, S.A.; Zeng, E.Y. China's water pollution by persistent organic pollutants. *Environ. Pollut.* **2012**, *163*, 100–108.
5. Shi, K.; Zhang, Y.; Zhu, G.; Qin, B.; Pan, D. Deteriorating water clarity in shallow waters: Evidence from long term MODIS and in-situ observations. *Int. J. Appl. Earth Obs.* **2018**, *68*, 287–297.
6. Liu, X.; Lee, Z.; Zhang, Y.; Lin, J.; Shi, K.; Zhou, Y.; Qin, B.; Sun, Z. Remote Sensing of Secchi Depth in Highly Turbid Lake Waters and Its Application with MERIS Data. *Remote Sens.* **2019**, *11*, 2226–2244.
7. Jiang, D.; Matsushita, B.; Setiawan, F.; Vundo, A. An improved algorithm for estimating the Secchi disk depth from remote sensing data based on the new underwater visibility theory. *ISPRS J. Photogramm.* **2019**, *152*, 13–23.
8. Li, T.; Zhu, B.; Cao, F.; Sun, H.; He, X.; Liu, M.; Gong, F.; Bai, Y. Monitoring Changes in the Transparency of the Largest Reservoir in Eastern China in the Past Decade, 2013–2020. *Remote Sens.* **2021**, *13*, 2570–2587.
9. Rodríguez-López, L.; Duran-Llacer, I.; González-Rodríguez, L.; Cardenas, R.; Urrutia, R. Retrieving Water Turbidity in Araucanian Lakes (South-Central Chile) Based on Multispectral Landsat Imagery. *Remote Sens.* **2021**, *13*, 3133–3148.
10. Cao, Z.; Duan, H.; Feng, L.; Ma, R.; Xue, K. Climate- and human-induced changes in suspended particulate matter over Lake Hongze on short and long timescales. *Remote Sens. Environ.* **2017**, *192*, 98–113.
11. McCullough, I.M.; Loftin, C.S.; Sader, S.A. Combining Lake and watershed characteristics with Landsat TM data for remote estimation of regional lake clarity. *Remote Sens. Environ.* **2012**, *123*, 109–115.
12. Maciel, D.A.; Barbosa, C.C.F.; Novo, E.M.L.d.M.; Flores Júnior, R.; Begliomini, F.N. Water clarity in Brazilian water assessed using Sentinel-2 and machine learning methods. *ISPRS J. Photogram.* **2021**, *182*, 134–152.

13. Wei, X.; Xu, W.; Bao, K.; Hou, W.; Su, J.; Li, H.; Miao, Z. A Water Body Extraction Methods Comparison Based on FengYun Satellite Data: A Case Study of Poyang Lake Region, China. *Remote Sens.* **2020**, *12*, 3875–3897.
14. Shang, S.; Lee, Z.; Shi, L.; Lin, G.; Wei, G.; Li, X. Changes in water clarity of the Bohai Sea: Observations from MODIS. *Remote Sens. Environ.* **2016**, *186*, 22–31.
15. Bonansea, M.; Rodriguez, M.C.; Pinotti, L.; Ferrero, S. Using multi-temporal Landsat imagery and linear mixed models for assessing water quality parameters in Río Tercero reservoir (Argentina). *Remote Sens. Environ.* **2015**, *158*, 28–41.
16. Kloiber, S.M.; Brezonik, P.L.; Olmanson, L.G.; Bauer, M.E. A procedure for regional lake water clarity assessment using Landsat multispectral data. *Remote Sens. Environ.* **2002**, *82*, 37–48.
17. Cillero Castro, C.; Domínguez Gómez, J.A.; Delgado Martín, J.; Hinojo Sánchez, B.A.; Cereijo Arango, J.L.; Cheda Tuya, F.A.; Díaz-Varela, R. An UAV and Satellite Multispectral Data Approach to Monitor Water Quality in Small Reservoirs. *Remote Sens.* **2020**, *12*, 1514–1546.
18. Siegel, D.A.; Behrenfeld, M.J.; Maritorena, S.; McClain, C.R.; Antoine, D.; Bailey, S.W.; Bontempi, P.S.; Boss, E.S.; Dierssen, H.M.; Doney, S.C.; et al. Regional to global assessments of phytoplankton dynamics from the SeaWiFS mission. *Remote Sens. Environ.* **2013**, *135*, 77–91.
19. Westergaard-Nielsen, A.; Christiansen, C.T.; Elberling, B. Growing season leaf carbon:nitrogen dynamics in Arctic tundra vegetation from ground and Sentinel-2 observations reveal reallocation timing and upscaling potential. *Remote Sens. Environ.* **2021**, *262*, 112512–112522.
20. Jorge, D.S.F.; Loisel, H.; Jamet, C.; Dessailly, D.; Demaria, J.; Bricaud, A.; Maritorena, S.; Zhang, X.; Antoine, D.; Kutser, T.; et al. A three-step semi analytical algorithm (3SAA) for estimating inherent optical properties over oceanic, coastal, and inland waters from remote sensing reflectance. *Remote Sens. Environ.* **2021**, *263*, 1125737–1112553.
21. Gupana, R.S.; Odermatt, D.; Cesana, I.; Giardino, C.; Nedbal, L.; Damm, A. Remote sensing of sun-induced chlorophyll-a fluorescence in inland and coastal waters: Current state and future prospects. *Remote Sens. Environ.* **2021**, *262*, 112482–112502.
22. Chen, J.; Wang, J.; Wang, Q.; Lv, J.; Liu, X.; Chen, J.; Li, N. Common fate of sister lakes in Hulunbuir Grassland: Long-term harmful algal bloom crisis from multi-source remote sensing insights. *J. Hydrol.* **2021**, *594*, 125970–125988.
23. Zheng, J.; Ke, C.; Shao, Z.; Li, F. Monitoring changes in the water volume of Hulun Lake by integrating satellite altimetry data and Landsat images between 1992 and 2010. *J. Appl. Remote Sens.* **2016**, *10*, 16–29.
24. Zhao, B.; Du, J.; Song, K.; Jacinthe, P.-A.; Xiang, X.; Zhou, H.; Yang, Z.; Zhang, L.; Guo, P. Spatio-temporal Variation of Water Heat Flux Using MODIS Land Surface Temperature Product over Hulun Lake, China During 2001–2018. *Chin. Geogr. Sci.* **2020**, *30*, 1065–1080.
25. Klein, I.; Dietz, A.J.; Gessner, U.; Galayeva, A.; Myrzakhmetov, A.; Kuenzer, C. Evaluation of seasonal water body extents in Central Asia over the past 27 years derived from medium-resolution remote sensing data. *Int. J. Appl. Earth Obs.* **2014**, *26*, 335–349.
26. Wang, Z.; Huang, N.; Luo, L.; Li, X.; Ren, C.; Song, K.; Chen, J.M. Shrinkage and fragmentation of marshes in the West Songnen Plain, China, from 1954 to 2008 and its possible causes. *Int. J. Appl. Earth Obs.* **2011**, *13*, 477–486.
27. Wang, Q.; Song, K.; Wen, Z.; Shang, Y.; Li, S.; Fang, C.; Du, J.; Zhao, F.; Liu, G. Long-term remote sensing of total suspended matter using Landsat series sensors in Hulun Lake, China. *Int. J. Remote Sens.* **2020**, *42*, 1379–1397.
28. Liu, Y.; Yue, H. Estimating the fluctuation of Lake Hulun, China, during 1975-2015 from satellite altimetry data. *Environ. Monit. Assess.* **2017**, *189*, 630–645.
29. Liang, L.; Li, C.; Shi, X.; Zhao, S.;Tian, Y.; Zhang, L. Analysis on the eutrophication trends and affecting factors in Lake Hulun, 2006-2015. *J. Lake Sci.* **2016**, *28*, 1265–1273. (In Chinese)
30. Roy, D.P.; Kovalskyy, V.; Zhang, H.K.; Vermote, E.F.; Yan, L.; Kumar, S.S.; Egorov, A. Characterization of Landsat-7 to Landsat-8 reflective wavelength and normalized difference vegetation index continuity. *Remote Sens. Environ.* **2016**, *185*, 57–70.
31. Hantson, S.; Huxman, T.E.; Kimball, S.; Randerson, J.T.; Goulden, M.L. Warming as a Driver of Vegetation Loss in the Sonoran Desert of California. *J. Geophys. Res-Biogeo.* **2021**, *126*, e2020JG005942.
32. Chander, G.; Markham, B.L.; Helder, D.L. Summary of current radiometric calibration coefficients for Landsat MSS, TM, ETM+, and EO-1 ALI sensors. *Remote Sens. Environ.* **2009**, *113*, 893–903.
33. Zhang, X.; Liu, L.; Chen, X.; Gao, Y.; Xie, S.; Mi, J. GLC_FCS30: Global land-cover product with fine classification system at 30 m using time-series Landsat imagery. *Earth Syst. Sci. Data* **2021**, *13*, 2753–2776.
34. McFeeters, S.K. The use of the Normalized Difference Water Index (NDWI) in the delineation of open water features. *Int. J. Remote Sens.* **2007**, *17*, 1425–1432.
35. Du, Y.; Zhang, Y.; Ling, F.; Wang, Q.; Li, W.; Li, X. Water Bodies' Mapping from Sentinel-2 Imagery with Modified Normalized Difference Water Index at 10-m Spatial Resolution Produced by Sharpening the SWIR Band. *Remote Sens.* **2016**, *8*, 354.
36. Singh, K.V.; Setia, R.; Sahoo, S.; Prasad, A.; Pateriya, B. Evaluation of NDWI and MNDWI for assessment of waterlogging by integrating digital elevation model and groundwater level. *Geocarto Int.* **2014**, *30*, 650–661.
37. Xu, H. Modification of normalised difference water index (NDWI) to enhance open water features in remotely sensed imagery. *Int. J. Remote Sens.* **2007**, *27*, 3025–3033.
38. Sun, F.; Sun, W.; Chen, J.; Gong, P. Comparison and improvement of methods for identifying waterbodies in remotely sensed imagery. *Int. J. Remote Sens.* **2012**, *33*, 6854–6875.
39. Xu, H. A Study on Information Extraction of Water Body with the Modified Normalized Difference Water Index (MNDWI). *J. Remote Sens.* **2005**, *9*, 589–595. (In Chinese)

40. Feyisa, G.; Meilby, H.; Fensholt, R.; Proud, S. Automated Water Extraction Index: A new technique for surface water mapping using Landsat imagery. *Remote Sens. Environ.* **2014**, *140*, 23–35.
41. Luo, Y.; Doxaran, D.; Vanhellemont, Q. Retrieval and Validation of Water Turbidity at Metre-Scale Using Pléiades Satellite Data: A Case Study in the Gironde Estuary. *Remote Sens.* **2020**, *12*, 946–968.
42. Lu, Q.; Si, W.; Wei, L.; Li, Z.; Xia, Z.; Ye, S.; Xia, Y. Retrieval of Water Quality from UAV-Borne Hyperspectral Imagery: A Comparative Study of Machine Learning Algorithms. *Remote Sens.* **2021**, *13*, 3928–3946.
43. Boruff, B.J.; Easoz, J.A.; Steve, D.; Jones; Landry, H.R.; Mitchem, J.D.; Cutter, S.L. Tornado hazards in the United States. *Clim. Res.* **2003**, *24*, 103–117.
44. Moore, T.W.; McGuire, M.P. Using the standard deviational ellipse to document changes to the spatial dispersion of seasonal tornado activity in the United States. *NPJ Clim. Atmos. Sci.* **2019**, *2*, 21–28.
45. Yu, Z.; Yang, K.; Luo, Y.; Yang, Y. Secchi depth inversion and its temporal and spatial variation analysis—A case study of nine plateau lakes in Yunnan Province of China. *Int. J. Appl. Earth Obs.* **2021**, *100*, 102344–102353.
46. Markogianni, V.; Kalivas, D.; Petropoulos, G.; Dimitriou, E. An Appraisal of the Potential of Landsat 8 in Estimating Chlorophyll-a, Ammonium Concentrations and Other Water Quality Indicators. *Remote Sens.* **2018**, *10*, 1018–1039.
47. Guo, X.; Wu, X.; Bing, Q.; Pan, Y.; Wang, Z.; Fu, Y.; Wang, D.; Liu, J. Study on Retrieval of Chlorophyll-a Concentration Based on Landsat OLI Imagery in the Haihe River, China. *Sustainability* **2016**, *8*, 758–779.
48. Soma, M.; Pimont, F.; Allard, D.; Fournier, R.; Dupuy, J.-L. Mitigating occlusion effects in Leaf Area Density estimates from Terrestrial LiDAR through a specific kriging method. *Remote Sens. Environ.* **2020**, *245*, 111836–111847.
49. Li, X.; Shen, H.; Feng, R.; Li, J.; Zhang, L. DEM generation from contours and a low-resolution DEM. *ISPRS J. Photogramm.* **2017**, *134*, 135–147.
50. Feng, L.; Hou, X.; Zheng, Y. Monitoring and understanding the water transparency changes of fifty large lakes on the Yangtze Plain based on long-term MODIS observations. *Remote Sens. Environ.* **2019**, *221*, 675–686.
51. Yang, K.; Luo, Y.; Chen, K.; Yang, Y.; Shang, C.; Yu, Z.; Xu, J.; Zhao, Y. Spatial–temporal variations in urbanization in Kunming and their impact on urban lake water quality. *Land. Degrad. Dev.* **2020**, *31*, 1392–1407.
52. Zia, H.; Harris, N.R.; Merrett, G.V.; Rivers, M.; Coles, N. The impact of agricultural activities on water quality: A case for collaborative catchment-scale management using integrated wireless sensor networks. *Comput. Electron. Agric.* **2013**, *96*, 126–138.
53. Caković, M.; Beloica, J.; Belanović Simić, S.; Miljković, P.; Lukić, S.; Baumgertel, A.; Schwaiger, F. Diffuse Pollution and Ecological Risk Assessment in Ludaš Lake Special Nature Reserve and Palić Nature Park (Pannonian Basin). *Forests* **2021**, *12*, 1461–1479.
54. Zhou, Q.; Wang, W.; Huang, L.; Zhang, Y.; Qin, J.; Li, K.; Chen, L. Spatial and temporal variability in water transparency in Yunnan Plateau lakes, China. *Aquat. Sci.* **2019**, *81*, 36–49.
55. Wang, W.; Zheng, B.; Jiang, X.; Chen, J.; Wang, S. Characteristics and Source of Dissolved Organic Matter in Lake Hulun, A Large Shallow Eutrophic Steppe Lake in Northern China. *Water* **2020**, *12*, 953–970.
56. Cheng, C.; Wei, Y.; Lv, G.; Xu, N. Remote sensing estimation of chlorophyll-a concentration in Taihu Lake considering spatial and temporal variations. *Environ. Monit. Assess.* **2019**, *84*, 191.
57. Zhang, Y.; Shi, K.; Zhou, Y.; Li, N. Remote sensing estimation of water clarity for various lakes in China. *Water Res.* **2021**, *192*, 116844.
58. Qing, S.; Cui, T.; Lai, Q.; Bao, Y.; Diao, R.; Yue, Y.; Hao, Y. Improving remote sensing retrieval of water clarity in complex coastal and inland waters with modified absorption estimation and optical water classification using Sentinel-2 MSI. *Int. J. Appl. Earth Obs.* **2021**, *102*, 102377–102392.
59. Yang, K.; Yu, Z.; Luo, Y.; Yang, Y.; Zhao, L.; Zhou, X. Spatial and temporal variations in the relationship between lake water surface temperatures and water quality—A case study of Dianchi Lake. *Sci. Total Environ.* **2018**, *624*, 859–871.
60. Gao, S.; Li, Z.; Chen, M.; Lin, P.; Hong, Z.; Allen, D.; Neeson, T.; Hong, Y. Spatiotemporal variability of global river extent and the natural driving factors revealed by decades of Landsat observations, GRACE gravimetry observations, and land surface model simulations. *Remote Sens. Environ.* **2021**, *267*, 112725–112739.
61. Qiao, B.; Zhu, L.; Yang, R. Temporal-spatial differences in lake water storage changes and their links to climate change throughout the Tibetan Plateau. *Remote Sens. Environ.* **2019**, *222*, 232–243.
62. Free, G.; Bresciani, M.; Pinardi, M.; Giardino, C.; Alikas, K.; Kangro, K.; Room, E.-I.; Vaiciute, D.; Bucas, M.; Tiskus, E.; et al. Detecting Climate Driven Changes in Chlorophyll-a Using High Frequency Monitoring: The Impact of the 2019 European Heatwave in Three Contrasting Aquatic Systems. *Sensors* **2021**, *21*, 6242–6260.
63. Xia, R.; Zhang, Y.; Critto, A.; Wu, J.; Fan, J.; Zheng, Z.; Zhang, Y. The Potential Impacts of Climate Change Factors on Freshwater Eutrophication: Implications for Research and Countermeasures of Water Management in China. *Sustainability* **2016**, *8*, 229–245.
64. Dong, Y.; Yin, D.; Li, X.; Huang, J.; Su, W.; Li, X.; Wang, H. Spatial–Temporal Evolution of Vegetation NDVI in Association with Climatic, Environmental and Anthropogenic Factors in the Loess Plateau, China during 2000–2015: Quantitative Analysis Based on Geographical Detector Model. *Remote Sens.* **2021**, *13*, 4380–4409.